

**Impedance Spectroscopy of $(\text{MnFe}_2\text{O}_4)_x/\text{CuTi-1223}$
Nanoparticles-Superconductor Composite**



By

Muhammad Naveed

(335-FBAS/MSPHY/F15)

Supervisor:

Dr. Muhammad Mumtaz

Assistant Professor

Department of Physics, FBAS,
IIU, Islamabad

Department of Physics

Faculty of Basic and Applied Sciences (FBAS)

International Islamic University Islamabad, Pakistan

(2017)





Accession No TH:18380V

MS
620.5
MUI

Nanotechnology.
Nanoparticles.
X-Ray diffraction



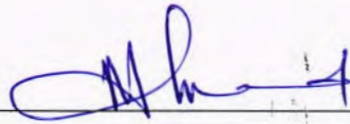
**Impedance Spectroscopy of $(\text{MnFe}_2\text{O}_4)_x/\text{CuTl-1223}$
Nanoparticles-Superconductor Composite**

By

Muhammad Naveed

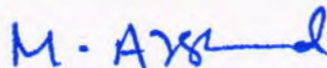
(335-FBAS/MSPHY/F15)

This Thesis submitted to Department of Physics International Islamic University,
Islamabad, for the award of degree of MS Physics.



CHAIRMAN
DEPT. OF PHYSICS
International Islamic University
Islamabad

Chairman Department of Physics
International Islamic University, Islamabad.



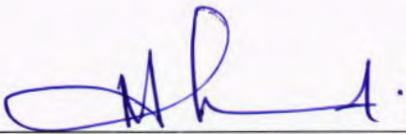
Dean Faculty of Basic and Applied Sciences
International Islamic University, Islamabad.

Final approval

It is certified that the work presented in this thesis entitled “Impedance Spectroscopy of $(\text{MnFe}_2\text{O}_4)_x/\text{CuTi-1223}$ Nanoparticles-Superconductor Composite” by Muhammad Naveed registration No. 335-FBAS/MSPHY/F15 fulfils the requirement for the award of degree of MS Physics from Department of Physics, FBAS, International Islamic University Islamabad, Pakistan.

Viva Voce Committee

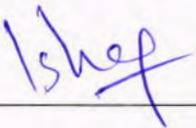
Chairman
(Department of Physics)



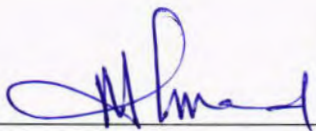
Supervisor



External Examiner



Internal Examiner



بِسْمِ اللَّهِ الرَّحْمَنِ الرَّحِيمِ

DEDICATED
To
My beloved Parents,
Brothers, Sisters.
Loving friends
and
Respected Teachers

Declaration of Originality

I, **Muhammad Naveed** Registration No. 335-FBAS/MSPHY/F15 student of MS Physics (Session 2015-2017), hereby declare that the work presented in the thesis entitled "**Impedance Spectroscopy of (MnFe₂O₄)/CuTi-1223 Nanoparticles-Superconductor Composites**" in partial fulfilment of MS degree in Physics from International Islamic University, Islamabad, is my own work and has not been published or submitted as research work or thesis in any form in any other university or institute in Pakistan or abroad.

Muhammad Naveed

(335-FBAS/MSPHY/F15)



Dated: _____

24 July 2017

Forwarding Sheet by Research Supervisor

The thesis entitled “Impedance Spectroscopy of $(\text{MnFe}_2\text{O}_4)_x/\text{CuTi-1223}$ Nanoparticles-Superconductor Composites” submitted by Muhammad Naveed (Registration No. 335-FBAS/MSPHY/F15) in partial fulfilment of MS degree in Physics has been completed under my guidance and supervision. I am satisfied with the quality of his research work and allow him to submit this thesis for further process to graduate with Master of Science degree from Department of Physics, as per International Islamic University, Islamabad rules and regulations.



Muhammad Mumtaz

Assistant Professor

Department of Physics

International Islamic University,
Islamabad

Dated: 24/07/2017

Acknowledgement

It gives me great pleasure to acknowledge the endowment of **ALLAH**, the most mighty and merciful, who made me able to accomplish this research work successfully. I offer my humblest and sincere words of thanks to his **Holy Prophet Muhammad (P.B.U.H)** who is forever a source of guidance and knowledge for humanity.

This work would have not been possible without the invaluable contributions of my individuals. First and foremost, I wish to thank my supervisor **Dr. Muhammad Mumtaz**, for all of his support, advice, and guidance during the whole period of my study. I would like to pay lot of appreciation to all my teachers who blessed me with knowledge and guidance.

I cannot forget the cooperation of my group members **Muhammad Imran, Liaqat Ali, Abrar Ahmed Khan, Badshah Amin** and others who facilitated my research work. I also pay special thanks to my colleagues **Abdul Saboor and Razaqat Ali Khan** for being very supportive and co-operative throughout my education career.

I especially want to acknowledge efforts and prayers of my father, mother, brothers in law, sisters and sisters in law and especially brothers **Muhammad Sharif and Muhammad Zafeer** for their love, care and support in my life, which has been directly encouraging me for my study. My parent's prayers are always a source of my success. Allah may bless my parents and family with long life, health and happiness. I thank again **ALMIGHTY ALLAH**, who listens and responds to my every prayer.

Muhammad Naveed

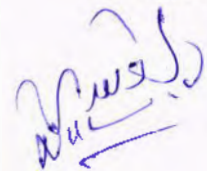


Table of Contents

List of figures	x
Nomenclature	xii
Abstract	xiv
Chapter 1: Introduction	1
1.1 Phenomenology	1
1.2 Complex Impedance	2
1.3 Impedance related functions	4
1.3.1 Nyquist Plot	5
1.3.2 Bode Plot	6
1.4 Relaxation phenomenon	7
1.4.1 Debye-type relaxation phenomenon	7
1.4.2 Non-Debye type relaxation phenomenon	7
1.5 History of Superconductors	7
1.6 CuTl-1223 Superconductor	9
Chapter 2 Literature review	11
2.1 Literature review	11
2.2 Motivation	15
Chapter 3: Synthesis and Characterization Techniques	16
3.1 Nanoparticle's Preparation	16
3.2 MnFe ₂ O ₄ nanoparticles synthesis	16
3.3 Superconductor synthesis	18
3.4 Synthesis of Cu _{0.5} Ba ₂ Ca ₂ Cu ₃ O _{10-δ} precursor	18
3.5 Synthesis of (MnFe ₂ O ₄) _x /CuTl-1223 nanoparticles-superconductor composite	19
3.6 Experimental techniques	21
3.6.1 XRD	21
3.6.1.1 Working principle	22
3.6.1.2 Applications of XRD	23
3.6.2 Scanning electron microscopy (SEM)	23
3.6.2.1 Components of SEM	24
3.6.3 Resistivity measurements by Four-probe method	25
3.6.4 Impedance analyzer	26
Chapter 4: Results and Discussion	28
4.1 X-Ray diffraction analysis (XRD)	28

4.2	SEM analysis.....	29
4.3	dc resistivity measurements (RT).....	29
4.4	Impedance analysis	30
4.4.1	Nyquist Plot	31
4.4.2	Activation Energy Calculation.....	33
4.4.3	Real Part of Impedance	35
4.4.4	Imaginary Part of Impedance	37
4.4.5	Non-Debye type relaxation phenomenon.....	39
4.4.6	ac-conductivity (σ_{ac}).....	41
Conclusion		43
Bibliography:.....		44

List of figures

Fig. 1.1: Sinusoidal Current Response in a Linear System.....	2
Fig. 1.2: Origin of Lissajous Figure.....	3
Fig. 1.3: Vector diagram of impedance.....	4
Fig. 1.4: equivalent RC-parallel circuit.....	5
Fig. 1.5: Nyquist Plot with Impedance Vector.....	5
Fig. 1.6: Bode plot of real and imaginary part of impedance verses frequency.....	6
Fig. 1.7: Kamerlingh Onnes (Left) discovery of superconductivity by Onnes (Right).....	8
Fig. 1.8: Schematic image is showing pairing of electrons in distorted lattice.....	8
Fig. 1.9: History of superconductor's development with year.....	9
Fig. 1.10: Lattice structure of CuTI-1223 crystal.....	10
Fig. 3.1: Flowchart of various methods for the preparation of nanoparticles.....	16
Fig. 3.2: schematic flowchart of sol-gel method for the synthesis of $MnFe_2O_4$ nanoparticles...17	17
Fig. 3.3: Schematic diagram of preparation of precursor.....	19
Fig. 3.4: flow chart of synthesis of $(MnFe_2O_4)_x/CuTI-1223$ Nanoparticles-Superconductor...20	20
Fig. 3.5: Schematic diagram of characterization techniques of sample.....	21
Fig. 3.6: Schematic diagram of X-ray diffractometer.....	22
Fig. 3.7: Mechanism of Bragg's law.....	23
Fig. 3.8: Schematic diagram of SEM setup.....	24
Fig. 3.9: Schematic diagram of four probe method.....	26
Fig. 3.10: Impedance analyser.....	27
Fig. 4.1: XRD spectra of $(MnFe_2O_4)_x/CuTI-1223$ nanoparticles-superconductor composites for $x=0$ and 2.0 wt.%. In the inset there are shown XRD spectrum of $MnFe_2O_4$ nanoparticles....28	28

Fig. 4.2: Resistivity vs temperature measurements of $(\text{MnFe}_2\text{O}_4)_x/\text{CuTi-1223}$ nanoparticles-superconductor composite samples for $x = 0$ and 2.0 wt.%. In the inset, there are shown SEM images of $(\text{MnFe}_2\text{O}_4)_x/\text{CuTi-1223}$ composites with (a) $x = 0$ and (b) 2.0 wt. %.....	30
Fig. 4.3: The electrical equivalent circuit for impedance.....	31
FIG. 4.4(a-c): The Nyquist plot of impedance between real part (Z') and imaginary part (Z'') for $(\text{MnFe}_2\text{O}_4)_x/\text{CuTi-1223}$ with (a) $x = 0$ at $T = 78 \text{ K}$ to 253 K , (b) $x = 1.0 \text{ wt.}\%$ at $T = 78 \text{ K}$ to 253 K , (c) $x = 2.0 \text{ wt.}\%$ at $T = 78 \text{ K}$ to 253 K	32
Fig. 4.5(a, b): (a). The plots of R_g/T versus $1000/T$ for $x = 0, 1.0$ and $2.0 \text{ wt.}\%$. (b). The plots of R_{gb}/T versus $1000/T$ for $1.0 \text{ wt.}\%$ and $x = 2.0 \text{ wt.}\%$. In the inset of (b) for $x = 0 \text{ }\%$	34
Fig. 4.6(a-c): Variation in real part (Z') of impedance versus frequency (40 Hz- 10 MHz) for $(\text{MnFe}_2\text{O}_4)_x/\text{CuTi-1223}$ with (a) $x = 0$ at $T = 78 \text{ K}$ to 253 K , (b) $x = 1.0 \text{ wt.}\%$ at $T = 78 \text{ K}$ to 253 K , (c) $x = 2.0 \text{ wt.}\%$ at $T = 78 \text{ K}$ to 253 K and in the insets there are shown the variation of Z' versus operating temperature (T) at frequency of 40 Hz.....	36
Fig. 4.7(a-c): Variation in imaginary part (Z'') of impedance versus frequency (40Hz- 10MHz) for $(\text{MnFe}_2\text{O}_4)_x/\text{CuTi-1223}$ with (a) $x = 0$ at $T = 78\text{K}$ to 253 K , (b) $x = 1.0 \text{ wt.}\%$ at $T = 78 \text{ K}$ to 253 K , (c) $x = 2.0 \text{ wt.}\%$ at $T = 78 \text{ K}$ to 253 K and in the insets there are shown the variation of Z''_{max} versus operating temperature (T).....	38
Fig. 4.8(a-c): The master curves of normalized parameters Z''/Z''_{max} versus f/f_{max} for $(\text{MnFe}_2\text{O}_4)_x/\text{CuTi-1223}$ nanoparticles-superconductor composite with (a) $x = 0$ at $T = 78 \text{ K}$ to 253 K , (b) $x = 1.0 \text{ wt.}\%$ at $T = 78 \text{ K}$ to 253 K , (c) $x = 2.0 \text{ wt.}\%$ at $T = 78 \text{ K}$ to 253 K	40
Fig. 4.9(a-c): Variation in ac-conductivity (σ_{ac}) versus frequency (40 Hz- 10 MHz) for $(\text{MnFe}_2\text{O}_4)_x/\text{CuTi-1223}$ with (a) $x = 0$ at $T = 78 \text{ K}$ to 253 K , (b) $x = 1.0 \text{ wt.}\%$ at $T = 78 \text{ K}$ to 253 K , (c) $x = 2.0 \text{ wt.}\%$ at $T = 78 \text{ K}$ to 253 K and in the insets there are shown the variation of σ_{ac} versus operating temperature (T) at frequency of 40 Hz.....	42

Nomenclature

CIS	Complex impedance spectroscopy
σ	AC Conductivity
Z'	Real part of impedance
Z''	Imaginary part of impedance
Z''_{max}	Maximum of Imaginary part of impedance
KWW	Kohlausch-Williams-Watts
β	Karlausch parameter
<i>FWHM</i>	Full width at half maximum
$\Phi(t)$	Time evaluation of electric field
τ	Relaxation time
ω	Angular frequency
f	Linear frequency
f_{max}	Maximum of linear frequency
R_{gb}	Grain boundary resistance
R_g	Grain resistance
C_g	Grain capacitance
C_{gb}	Grain boundary capacitance
<i>SEM</i>	Scanning electron microscope
<i>XRD</i>	X-ray diffraction
<i>HTSCs</i>	High temperature superconductors
<i>BCS</i>	Bardeen Cooper and Schrieffer
E_c	Activation energy of conduction

A_0	Pre-exponential factor
$CuTl$	Copper Thallium
YBCO	Yttrium Barrium Copper Oxide
T_c	Critical temperature
J_c	Critical current density
H_c	Critical megnatic field

Abstract

Manganese ferrite (MnFe_2O_4) nanoparticles and $\text{Cu}_{0.5}\text{Tl}_{0.5}\text{Ba}_2\text{Ca}_2\text{Cu}_3\text{O}_{10.8}$ (CuTI-1223) superconducting phase were prepared by sol-gel and solid-state reaction methods, respectively. MnFe_2O_4 nanoparticles were added in CuTI-1223 superconducting matrix to get $(\text{MnFe}_2\text{O}_4)_x/\text{CuTI-1223}$ ($x = 0 \sim 2.0$ wt.%) composites. Different experimental techniques like XRD, SEM, R-T measurements and Impedance spectroscopy were used to characterize these composites. It was observed that crystal structure of host CuTI-1223 phase remained unaltered after addition of MnFe_2O_4 nanoparticles, which indicated about the occupancy of these nanoparticles at grain-boundaries. The value of T_c^{onset} (K) showed over all decreasing trend with inclusion of MnFe_2O_4 nanoparticles, which may be attributed to spin-charge reflection and trapping of charge carriers due to presence of these magnetic nanoparticles at grain-boundaries of CuTI-1223 phase. In complex impedance spectroscopy (CIS), role of MnFe_2O_4 nanoparticles addition at the grain-boundaries of the host CuTI-1223 phase was investigated. The decrease in impedance (Z) with increasing temperature witnessed the occurring of thermally activated processes in this system. Higher value of activation energy at grain-boundaries showed that the grain-boundaries are more resistive than grains due to non-stoichiometric distribution of oxygen and dangling bonds at grain-boundaries. The impedance master curves indicated that the distribution of relaxation time (dynamic process) is nearly temperature independent. The decrease in ac-conductivity with increasing content of these nanoparticles indicated the enhancement of space charges at grain-boundaries.

Chapter 1: Introduction

1.1 Phenomenology

Complex impedance spectroscopy (CIS) appears destined to play an important role in fundamental, applied physics, chemistry and material sciences. CIS is useful tool to characterize various materials. The main advantages of this technique are: (i) It uses an ac-signal of small amplitude to probe the specimen. (ii) This technique has the ability to make proper separation among the bulk grains, grain-boundaries with electrode-interface properties between grain-boundaries and grain along with relaxation processes. (iii) It is method of choice for the development of electrical engineering for electrical circuit analysis of materials in which overall behavior is determined by number of strongly coupled processes. This technique is useful to separate the contributions from bulk (grain) and grain-boundaries to understand charge transport properties of polycrystalline materials that have different relaxation time in the frequency domain [1,2]. In present time, impedance spectroscopy is gaining importance in superconducting ceramics for information regarding the mechanism of conductivity, movement of electrons in superconductors at various temperatures, which can be useful to understand the superconducting phenomenon. Cuprates superconductors have vast applications in technical field such as power transmission lines, Josephson junction and electronic devices. Therefore, CIS has received the great deal of attention for understanding and explanations of electric and dielectric behaviour in superconducting materials.

In this chapter we aim to discuss about definition of Impedance, its related plots, applications and working background of impedance spectroscopy IS for materials scientist or engineers, who wishes to apply this technique as a method of analysis of dielectric materials. We have aim to describe the basics of superconductivity along with high temperature superconductors HTSCs. We will concentrate on intrinsically conductive systems, data presentation methods, relaxation phenomenon i.e. Debye type and non-Debye type phenomenon in dielectric materials as well.

1.2 Complex Impedance

Resistance is a general term which mostly used in physics. It is simply an opposition for electrical current to flow in an electric circuit element. According to Ohm's law resistance is simply the ratio of applied voltage to current flow in circuit and is given by

$$R = \frac{E}{A} \quad \dots\dots\dots (1)$$

This well-known relation is valid for only one circuit component. An ideal resistor contains following properties:

- It obey Ohm's Law any value of applied voltage and current.
- The resistance of ideal resistor is independent upon frequency.
- For ideal resistor the applied voltage signals and current both are in phase [3].

But in real world many electric circuits or components have complex network. These outcomes forced a new term that we use impedance to solve complex network. Electric impedance usually caused in circuit when we apply AC signal to any circuit element and then measure the flow of current in circuit.

To understand the concept of impedance we assume that we apply a sinusoidal AC voltage to any circuit element then current flow in circuit due to applied electric potential will also be a sinusoidal with same frequency but with phase shift of angle (Φ) is shown in Fig. 1.1

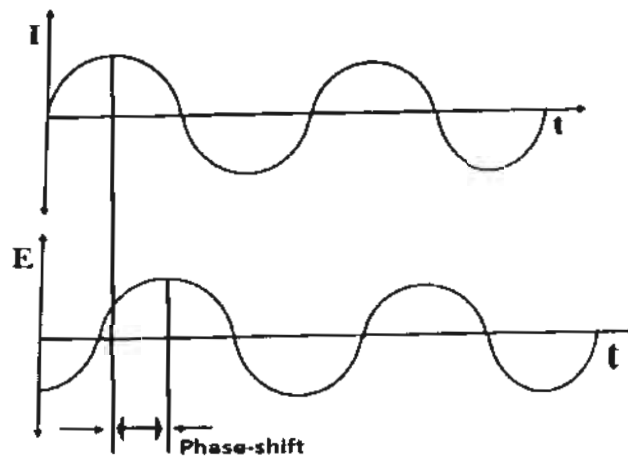


Figure 1.1: Response of Current to applied AC signal in a Linear System [4]

Electric potential as a function of time of applied AC signal has the form,

$$E_t = E_o \sin(\omega t) \dots \dots \dots (2)$$

here, E_t is electric potential at any time t , E_o is the amplitude of AC signal and ω is angular frequency.

In linear system, the response of current I_t to applied signal is in the form,

$$I_t = I_o \sin(\omega t + \phi) \dots \dots \dots (3)$$

Where I_o is amplitude and ϕ is the phase shift. These two equations allows us to calculate impedance by applied Ohm's law as:

$$Z = \frac{E_t}{I_t} = \frac{E_o \sin(\omega t)}{I_o \sin(\omega t + \phi)} = Z_o \frac{\sin(\omega t)}{\sin(\omega t + \phi)} \dots \dots \dots (4)$$

Impedance is therefore represented as Z_o . If we plot a graph between applied AC voltage E_t and the response of current I_t then the result is an oval as shown in Fig. 1.2.

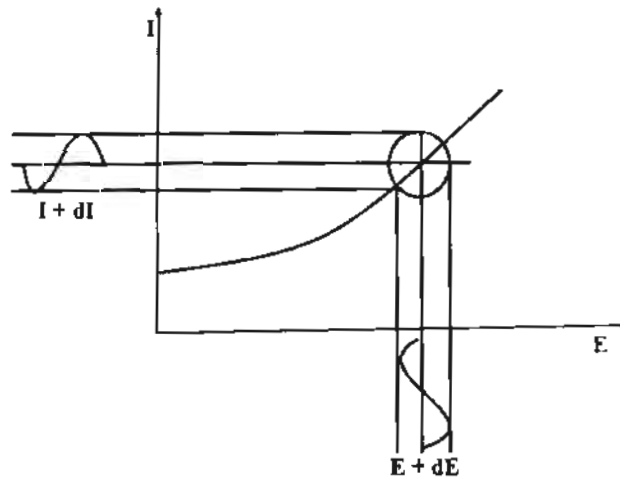


Figure 1.2: Origin of Lissajous Figure

In 1880s Oliver Heaviside the very first time give the concept of impedance, and the very soon complex representation in term of vector diagram was done by A. E. Kennelly and C. P. Steinmetz. The word Impedance is more general concept than resistance, therefore, impedance spectroscopy can be considered as branch of the tree in electrical engineering. Electrical impedance is the combined effect of resistance and reactance that oppose the current to flow in the circuit, when AC signal is applied [5-6]. The opposition caused by these two effects is collectively referred as resistance and reactance. In which resistance form real part in complex plan, while reactance forms the imaginary part. The symbolic representation of impedance is usually Z and in Cartesian form the impedance is defined as:

$$Z = R_{\text{real}} + iX_{\text{imaginary}} \dots\dots\dots(5)$$

Where R_{real} is the resistance and X_{imag} is the reactance. The graphical representation of complex impedance is shown in Fig. 1.3

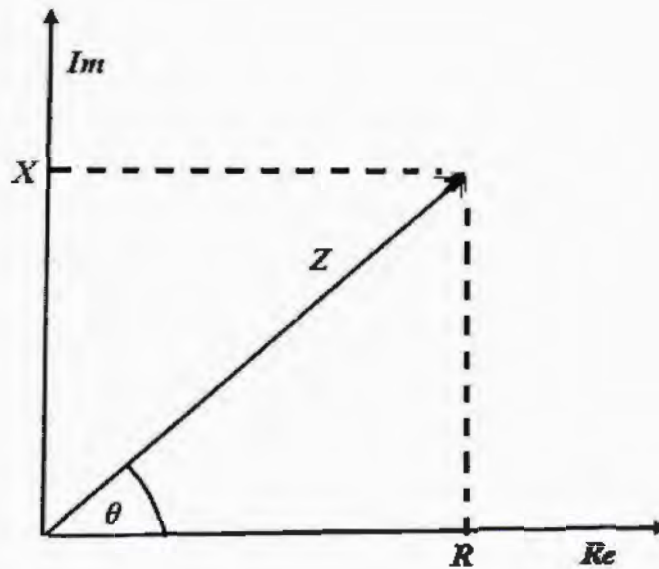


Fig.1.3: Vector diagram of impedance

1.3 Impedance related functions

Complex impedance data is usually represented as Z' - Z'' plots in which Z' is a real term and Z'' is imaginary term of complex impedance at various frequencies. Impedance is a complex quantity and is real when $\theta = 0$ and thus purely resistive behaviour. In this case impedance is frequency independent. For a pure capacitance C impedance depends upon the applied frequency of ac signal. A holistically connection between real and imaginary part of impedance when they are frequency dependent [7]. By physical meaning all the plots of impedance can be understand through equivalent RC - parallel circuit as shown in Fig. 1.4.

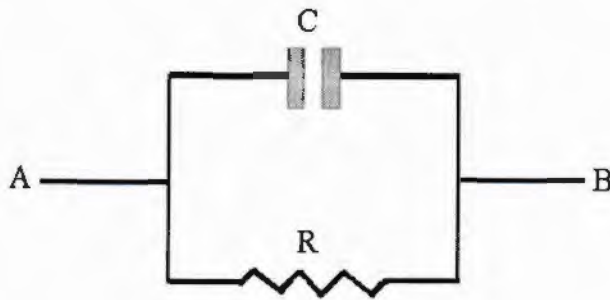


Fig. 1.4: RC-parallel circuit for understanding impedance

The complete solution of this circuit can be expressed as:

$$Z = \frac{R}{1+i\omega\tau} \dots\dots\dots (6)$$

Where $\tau = RC$ is time constant and ω is angular frequency.

1.3.1 Nyquist Plot

When equation (6) is plot in complex plane such a way that the real part (resistance) of impedance is taken along x-axis and the imaginary part (reactance) is along y-axis we obtained a semicircle called "Nyquist Plot" as shown in Fig 1.5. The intercept of this semicircle gives value of resistance R on the real axis [8]. The right intercept gives the impedance at low frequency and left intercept gives value of impedance for high frequency. The maxima of this semicircle gives resonance frequency which corresponds to $\omega\tau = 1$. angle between Z with x-axis, is known as phase angle.

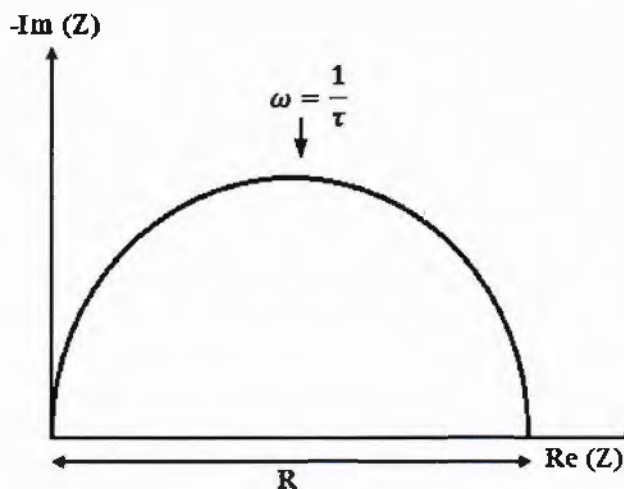


Fig. 1.5: Nyquist Plot with Impedance Vector

1.3.2 Bode Plot

Another most popular presentation of impedance data with applied frequency is known as the Bode Plot. This can also be understood from equation (6), after taking conjugate of that equation we obtained following equation.

$$Z = \frac{R}{1+\omega^2\tau^2} - i \frac{R\omega\tau}{1+\omega^2\tau^2} \dots\dots\dots (7)$$

Separating the real (Z') and imaginary part (Z''), we get

$$Z' = \frac{R}{1+\omega^2\tau^2} \dots\dots\dots (8)$$

$$Z'' = i \frac{R\omega\tau}{1+\omega^2\tau^2} \dots\dots\dots(9)$$

From equation (8) and (9), if we plot a graph between Z' and Z'' versus frequency we obtained a graph called bode plot as shown in Fig. 1.6. The graphs shows that at low frequency the resistive properties is more prominent and capacitive behavior is negligible. At the intersection point where $\omega\tau = 1$ is the resonance frequency where the system is in phase with applied field [8-10].

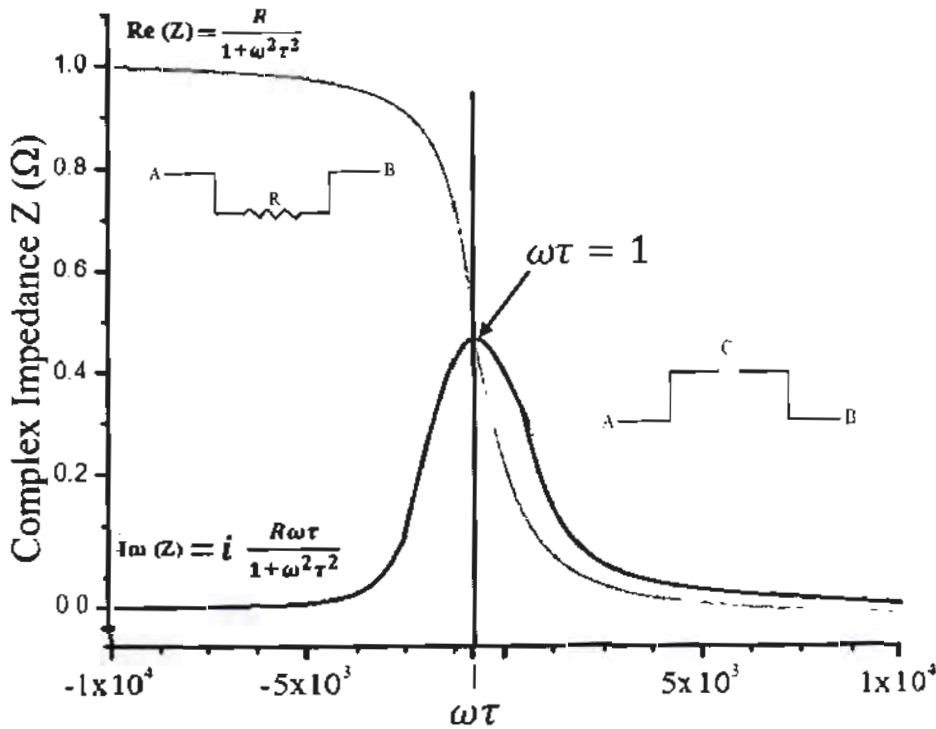


Fig. 1.6: Bode plot between Z' and Z'' verses frequency.

1.4 Relaxation phenomenon

In physics, the term relaxation refers to re-gain equilibrium position after perturbation the system. Therefore, any relaxation process can be understood by its relaxation time τ . But in case of dielectric materials the electric polarization of material depends upon applied field E . If electric field changes then polarization in material also changes and system wants to relax in a new equilibrium position. The dielectric relaxation is due to lag in response of material's polarization to applied field [12-15]. The dielectric relaxation time is related to the conductivity of material. Therefore, to investigate the conduction mechanism in materials dielectric relaxation time is an important parameter for understanding. Relaxation phenomenon is of two types.

1.4.1 Debye-type relaxation phenomenon

In Debye relaxation process all dipoles in the system relax with the same relaxation time (single relaxation time approximation). Ideal Debye relaxation has no practical application except in liquids and perfect crystal.

1.4.2 Non-Debye type relaxation phenomenon

But real materials usually exhibit broad relaxation time distribution and can be characterized by a pre-exponential factor. To understand the concept of Debye type and non-Debye type relaxation phenomenon we used the concept of Kohlrausch – Williams - Watts (KWW) function i.e.

$$\phi(t) = e^{-\left(\frac{t}{\tau}\right)^\beta} \text{----- (10)}$$

Where $\phi(t)$ is the time evolution of applied AC field exposed to the sample, and β is Kohlrausch parameter, which can be calculated by the relation $\beta = 1.14/\text{FWHM}$. If the value of $\beta = 1$ then material has single relaxation (Debye type) nature. If the value of β less than 1 then material has multi-Debye nature [11,16].

1.5 History of Superconductors

In 1911, Kamerlingh Onnes discovered a strange phenomenon in his laboratory. He was investigating resistivity at very low temperature when he observed the electrical resistance of different metals like lead, tin and mercury suddenly vanishes completely at sufficiently low temperatures. As example resistance of Mercury at 4.1 K as shown in Fig. 1.7. He was able to analyze pure sample of mercury as it was easy to prepare by condensation.

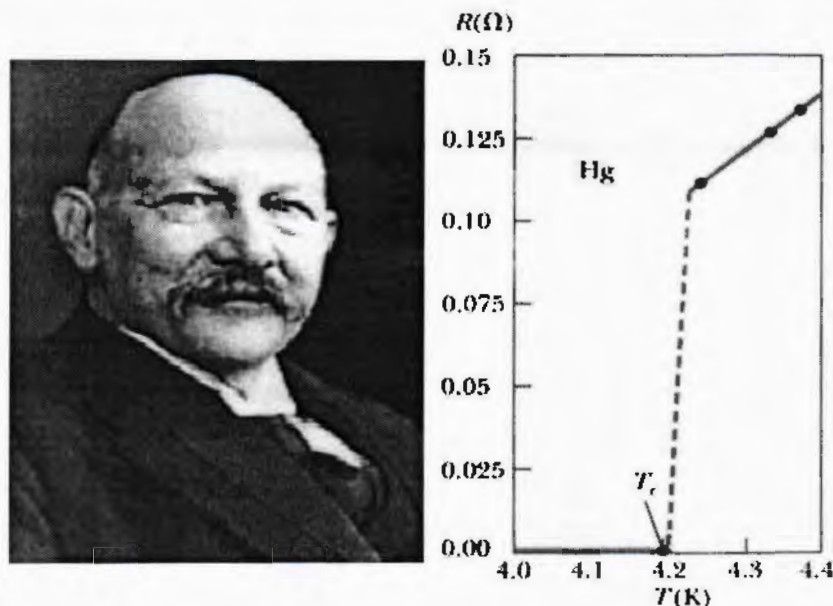


Fig. 1.7: Kamerlingh Onnes (Left) discovery of superconductivity by Onnes (Right) [17].

Two decades after the discovery of the superconductors, the perfect diamagnetic property of superconductor was found by Meissner and R. Ochsenfeld. This fundamental property of superconductors called Meissner effect. First theoretical explanation on mechanism of superconductivity was introduced by Bardeen, Cooper and Schrieffer known as BCS theory in 1957. They emphasized on the presence of two bodies shows attraction between charge carriers as a prerequisite for a Bose-Einstein condensation. According to this theory electrons just above the fermi-level shows attraction rather than repulsion by interaction with lattice phonons. These electrons combined to form integer spin called boson. They are responsible for superconductivity. Latter on, Bardeen solved the many body system problem for complete understanding.

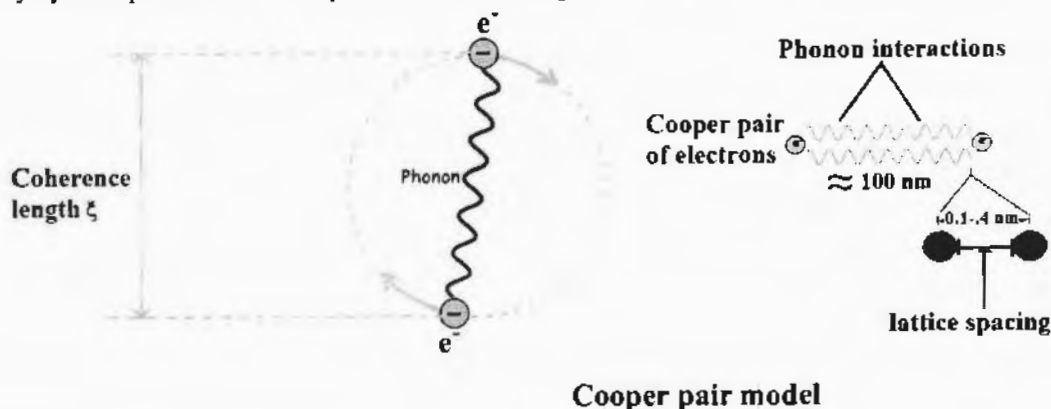


Fig. 2.8: cooper pair formation due to phonon interactions with electrons.

BSC theory was only applicable for those superconductors whose critical temperature below 35 K. In 1986, George Bednorz and Alex Muller performed an outstanding experiment. They prepared a ceramic superconductor based upon Barium, Lanthanum, Copper and Oxygen La-Ba-Cu-O with a critical temperature 35 K [18]. Further research on new ceramic bulk superconductors (Y-Ba-Cu-O) was carried out with a transition temperature of 92 K. presently, transition temperature is around 165 K in some materials.

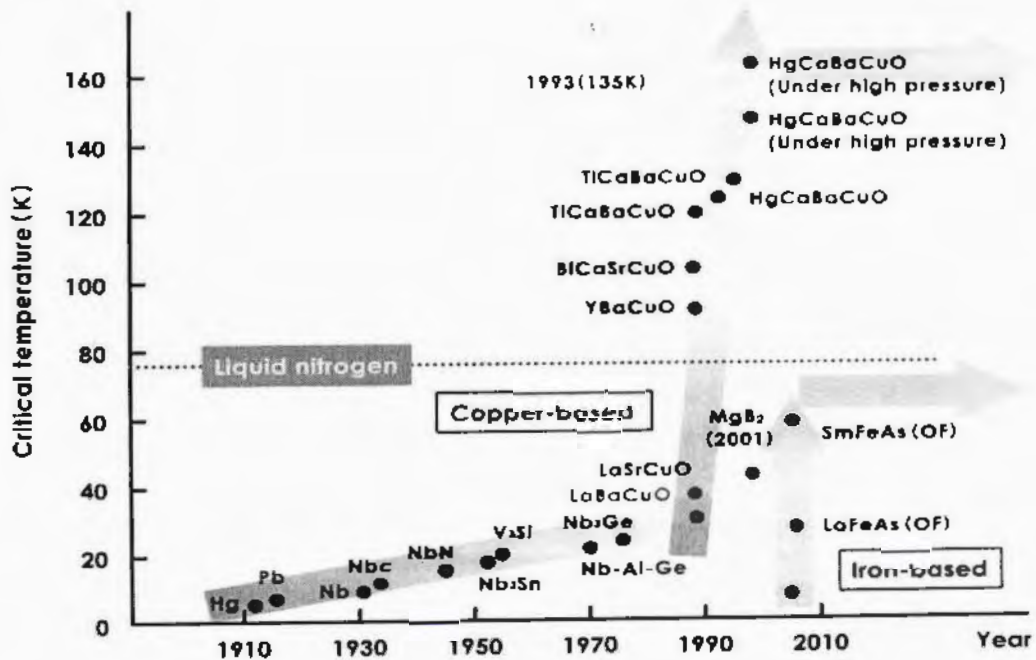


Fig. 1.9: Detailed history of superconductors from discovery to till.

1.6 CuTl-1223 Superconductor

Cu and Tl-based superconductors is most attractive two different families of HTSCs. Therefore, $(\text{Cu}_{0.5}\text{Tl}_{0.5})\text{Ba}_2\text{Ca}_{n-1}\text{Cu}_n\text{O}_{2n+4-\delta}$, based family of superconductor is one of the most important candidate for researchers due to its vast applications. CuTl-1223 matrix of $(\text{Cu}_{0.5}\text{Tl}_{0.5})\text{Ba}_2\text{Ca}_{n-1}\text{Cu}_n\text{O}_{2n+4-\delta}$ family has a great deal of interest due to its desired potential technological aspects. The unit cell of CuTl-1223 based superconductors is shown in Fig. The unit cell shows the two CuO_2 planes considered as charge reservoir and are responsible for superconductivity. CuTl-1223 based superconductor belong to $P4/mmm$ space group with tetragonal structure. The two sides of unit cell are equal i.e ($a = b = 4.37\text{\AA}$) and the third side is greater ($c = 14.82\text{\AA}$).

Chapter 2

Literature review

2.1 Literature review

Since the discovery of CuTl-based high temperature superconductors, a lot of efforts have been done with addition or substitution by different nanostructures to enhance electrical and magnetic properties. In spite of the fact that the cuprates superconductors have extensively been characterized but still no work have been reported on the frequency and temperature dependent impedance properties to make proper separation among the bulk grains, grain-boundaries with electrode-interface properties between grain-boundaries and grains. The $\text{Cu}_{0.5}\text{Tl}_{0.5}\text{Ba}_2\text{Ca}_2\text{Cu}_3\text{O}_{10.8}$ superconductor is an attractive candidate due to low anisotropy, high critical temperature (T_c), and current density (J_c). CIS is useful technique for studying the information regarding movement of carriers in superconductors at various temperatures, which may be useful in understanding the superconducting phenomenon. High temperature superconductors have vast applications in technical field such as robotic, power transmission lines, Josephson junction and electronic devices. This method helps to make proper separation among the bulk grains, grain-boundaries with electrode-interface properties between grains and grain-boundaries. Therefore, cuprates superconductors have received the great deal of attention due to their potential technological aspects.

B. Bahera *et al.* [20] studied the impedance spectroscopy of polycrystalline $\text{NaBa}_2\text{V}_5\text{O}_{15}$ sample which belongs to the family of tungsten bronze. The electrical diagnostic was carried out by impedance spectroscopic technique. Frequency and temperature dependence on impedance parameters with conductivity of material was investigated at various temperatures. In Nyquist plot the decrease in bulk resistance as a function of temperature was observed, which shows the semi-conducting behavior of the material. Spreading of peaks was observed which indicated the temperature dependence on the relaxation time. This spreading of relaxation time clearly due to the non-Debye type nature of material. At high frequency all the curves merge regardless of operating temperatures is due to the release of space charges.

G. Liu *et al.* [21] studied the impedance related parameters of niobium and aluminum Co-doped TiO_2 i.e. $(\text{Nb}_{0.5}\text{Al}_{0.5})_x\text{Ti}_{1-x}\text{O}_2$ ($x = 0, 0.01, 0.05, 0.1, 0.15$ wt.%) ceramics at various operating temperatures and by varying frequency. A significance increasing trend was observed in dielectric properties of (Nb + Al) Co-doped TiO_2 over a wide range of frequencies as compared to pure TiO_2 . The current density increased nonlinearly with applied electric field, conductivity increase with both increase in temperature and frequency. They two different

temperatures complex impedance spectroscopy was observed and different results were found. The annealing samples in oxygen environment contains the maximum resistance while those samples which were annealed in the presence of nitrogen environment possessed the minimum resistive behavior. The grain's conductivity was improved due to the additional electrons created.

B. B. Mohanty *et al.* [22] studied the effect of temperature on impedance properties of the polycrystalline sample of $\text{Ba}_5\text{GdTi}_3\text{V}_7\text{O}_{30}$. They observed complex impedance plots get depressed and their center of the arc lie below the real axis (Z') which confirms the polydispersive (multi-Debye type) nature of dielectric relaxation in BGTV. With the increasing temperature the decrease in bulk resistance of material exhibit the NTCR behavior of material.

S. P. Yadav *et al.* [23] studied the impedance along with dielectric and magnetic properties of $(\text{Co}_{1-x}\text{Mn}_x\text{Fe}_2\text{O}_4)$. They used ceramic method to synthesized the manganese substituted cobalt ferrite sample $(\text{Co}_{1-x}\text{Mn}_x\text{Fe}_2\text{O}_4)$ with ($x= 0, 0.1, 0.2, 0.3, 0.4, 0.5$ wt.%). They reported the effect of addition of Mn on impedance, magnetic and dielectric properties of cobalt ferrite composite. They studied the frequency dependent dielectric permittivity, loss tangent and impedance in the range from 20Hz to 10^6 Hz. They observed that there was only one semicircle in the cole-cole (imaginary part of the complex impedance versus real part) plot of all sample, which indicated the dominant grain boundary contribution in the conduction mechanism. Several models have been reported to be used for interpreting the results of complex impedance measurement on ferrites.

K. Kumari *et al.* [24] investigated the impedance related parameters of $(\text{Na}_{0.5}\text{Bi}_{0.5})(\text{Zr}_{0.25}\text{Ti}_{0.75})\text{O}_3$ lead-free ceramic polycrystalline sample with increasing frequency from 0.1 kHz to 1 MHz by operating temperature from 30 – 500°C. With the increasing both frequency and temperature the value of real part of impedance decreased which suggest the contribution of both grain and grain boundaries. The decrease in semicircle of Nyquist plot with increasing temperatures show the NTCR behavior. From cole-cole master curve the value of FWHM was found to be greater than 1.14, this shows the non-Debye (multi-Debye) response of material. AC conductivity increased with the rise in temperature and frequency, and Z' values for all temperatures merge above 100 kHz.

S. Nasri *et al.* [25] Studied the complex impedance, dielectric properties and conduction mechanism of $\text{La}_{0.5}\text{Ba}_{0.5}\text{FeO}_{3-\delta}$ frequency domains from few Hz to 7 MHz with 278 K to 573 K operating temperatures. They synthesized the sample by sol-gel method. They observed only one semi-circular arc at all temperatures which indicated the response of grain materials toward electrical processes, and the decreasing radius of the arcs with increasing

temperature suggested the insulating or semiconducting type nature of $\text{La}_{0.5}\text{Ba}_{0.5}\text{FeO}_{3-\delta}$ material. Overall increasing behavior of real part of impedance was observed with increasing temperatures, while imaginary part of impedance initially found to increase, attaining a peak at Z''_{max} and then decreased with frequency and temperature. They observed that the average peak position Z''_{max} shift to higher frequency indicated the increase in conductivity of materials which suggests a spread of relaxation time in the system due to hopping mechanism.

P. S. Sahoo *et al.* [26] investigated the modulus and impedance spectroscopy of barium strontium samarium vanadium ($\text{Ba}_4\text{SrSmTi}_3\text{V}_7\text{O}_{30}$) as functions of frequency at various temperatures. The complex impedance plot was depressed with increase in temperature probably due to decrease in the total resistance of material as a result of contribution of grain-boundaries upon increasing temperatures. This observation indicates that the electrical properties of material can be controlled by its microstructure. By increasing temperatures it was found that the real part of impedance decreases which indicates semiconducting (NTCR) type nature of the material. The shifting in peaks was found in imaginary part of impedance clearly the result of spreading of relaxation time. These outcomes showed that by this microstructure we can controlled the electrical properties of this material.

S.A Nediil' ko *et al.* [27] were studied the temperature dependent electrical properties of Barium cuprates $\text{BaCuO}_{2+\delta}$ with the frequency ranges of 5 Hz to 10^5 Hz by applying impedance spectroscopy. It was observed that value of Nyquist plot get depressed which is due to the semiconducting nature of barium cuprates. The decrease in real as well as imaginary part of impedance with operating temperatures is due to the release of space charge (space charge polarization) present at grain-boundaries, causes the reduction of some barriers in Barium cuprates sample.

J. Jose *et al.* [28] studied the electrical analysis of effect of grain-boundaries of ZnO-Ag nanocomposites by using impedance spectroscopy. They applied physical model to understand the effect of grains and grain-boundaries on the impedance properties of nanocomposites. The two semicircles were obtained in Nyquist plot whose centre lie below the real axis shows non-Debye nature of material. The decrease in imaginary part with the rise of temperature was observed which is due to the releasing of trapped carriers across boundaries.

J. Bashir *et al.* [29] investigated the complex impedance spectroscopy of $\text{Sr}_2\text{CoNbO}_6$ (SCNO) and $\text{Ba}_2\text{CoNbO}_6$ (BCNO) double perovskites at room temperatures with frequencies (1 Hz – 10 MHz), to estimate the effect of grains, grain boundary and interface on the charge transport phenomenon in perovskite materials. Complex impedance spectrum of both materials was depressed semicircles with SCNO showing more depression than BCNO. The depressed

semicircles showed about spread of relaxation time whereas broadness and asymmetric form of the Z'' peaks suggest at least two relaxation times. This is also clear from the M' and M'' spectrum where two relaxation processes can be resolved.

J. E. F. S. Rodrigues *et al.* [30] diagnostic the electrical analysis of $\text{Ba}_2\text{BiTaO}_6$ ceramic with varying both frequency at temperature from ($25^\circ\text{C} - 500^\circ\text{C}$) by using complex impedance spectroscopy. The depressed semicircles in Nyquist plot showed thermally activated process in material. And the shifting of peaks indicated about spread of relaxation time. The results clearly shows that electrical conduction of ($\text{Ba}_2\text{BiTaO}_6$) sample was due to hopping mechanism and oxygen vacancies.

L. Essaleh *et al.* [31] used the impedance spectroscopy to analyse the electrical properties of bulk p- CuIn_3Se_5 material of semi-conducting nature over a frequencies ranges from 20 to 1 MHz at temperatures (308 K - 350 K). The Nyquist plots (i.e. Z'' versus Z') were found to be depressed with the rise of temperature which clearly conform the NTCR behaviour of the sample. Decrease in relaxation time with increasing temperature was observed showed the temperature dependence on the relaxation time of material. With the raise in temperature values of calculated resistances decreased for both grains and grain-boundaries which show agreement with the Arrhenius law.

J. L. Acosta *et al.* [32] were investigated the ionic conductivity of $\text{YBa}_2\text{Cu}_3\text{O}_x$ via AC impedance spectroscopy. In the tetragonal regime, the ionic conductivity was observed to be independent upon oxygen partial pressure environment and calculated activation energy was found around $2.46 \pm 0.05\text{eV}$. A little dependence of oxygen partial pressure was found in the orthorhombic regime with activation energy of $2.46 \pm 0.05\text{eV}$.

F. E. Casallas *et al.* [33] were study the temperature dependence of electric response of $\text{La}_2\text{SrFe}_2\text{CoO}_9$ triple complex perovskite by using impedance spectroscopy with frequency ranges from 10.0 Hz up to 0.1 MHz. The decrease in both real and imaginary part of impedance with increasing temperature was observed. This decrease in total impedance in the sample is due to the release of trap charges at grain-boundaries. This is a good agreement of linear increase in ac conductivity in material by varying operating temperature.

2.2 Motivation

After the detailed literature survey, we come to know that till no work is reported on the impedance properties of CuTi-1223 matrix, to get information about the conduction mechanism and contribution of grains and grain-boundaries. Therefore, the main aim of this study is tuning the conduction mechanism and impedance related parameters of CuTi-1223 matrix by the addition of content of MnFe_2O_4 nanoparticles by varying frequency from few Hz to 100 MHz at various operating temperatures. This may be useful for technological aspects.

Chapter 3: Synthesis and Characterization Techniques

3.1 Nanoparticle's Preparation

Two different approaches are used to synthesis nanoparticles. One is top down approach in which bulk materials are reduced in nanometers range to get nanoparticles. The disadvantage of this method is the distribution of broad size of nanoparticles. The overall methods of preparation of nanoparticles is given in the flowchart Fig. 3.1. In chemical method, atoms and molecules are nucleate each other to get desired nanoparticles. The advantage of this approach is to control the size of nanoparticles as desired. But in our case sol-gel method is used for the synthesis of MnFe_2O_4 nanoparticles.

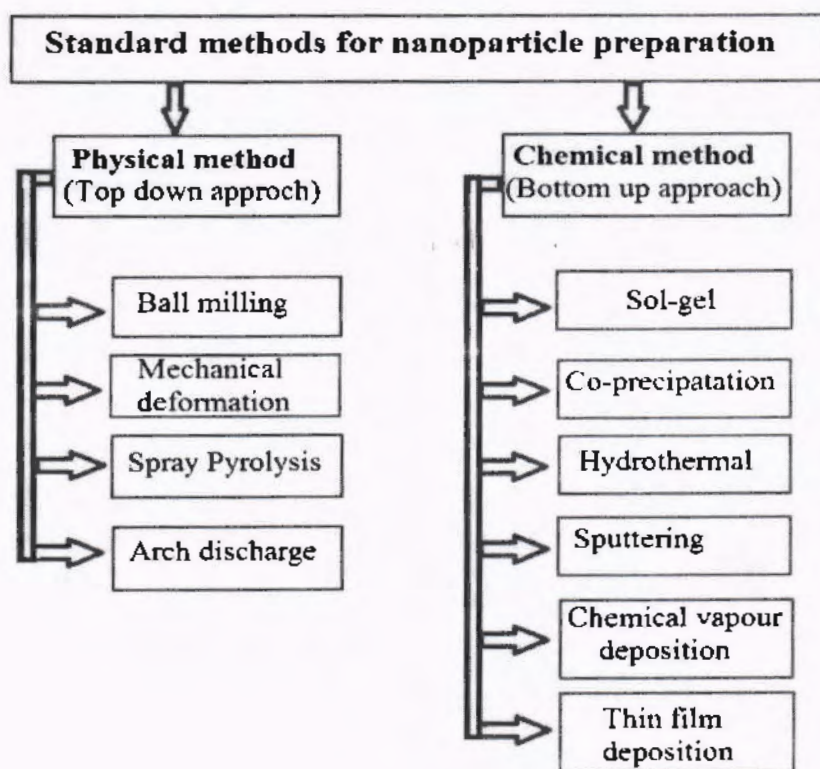


Fig. 3.1: Flowchart of various methods for the preparation of nanoparticles.

3.2 MnFe_2O_4 nanoparticles synthesis

We used sol-gel method to synthesized MnFe_2O_4 nanoparticles. Sol gel process is a chemical approach often used in material science and ceramic engineering field to fabricate the nanomaterials through solution. The flow chart of sol-gel method is shown in Fig. 3.2

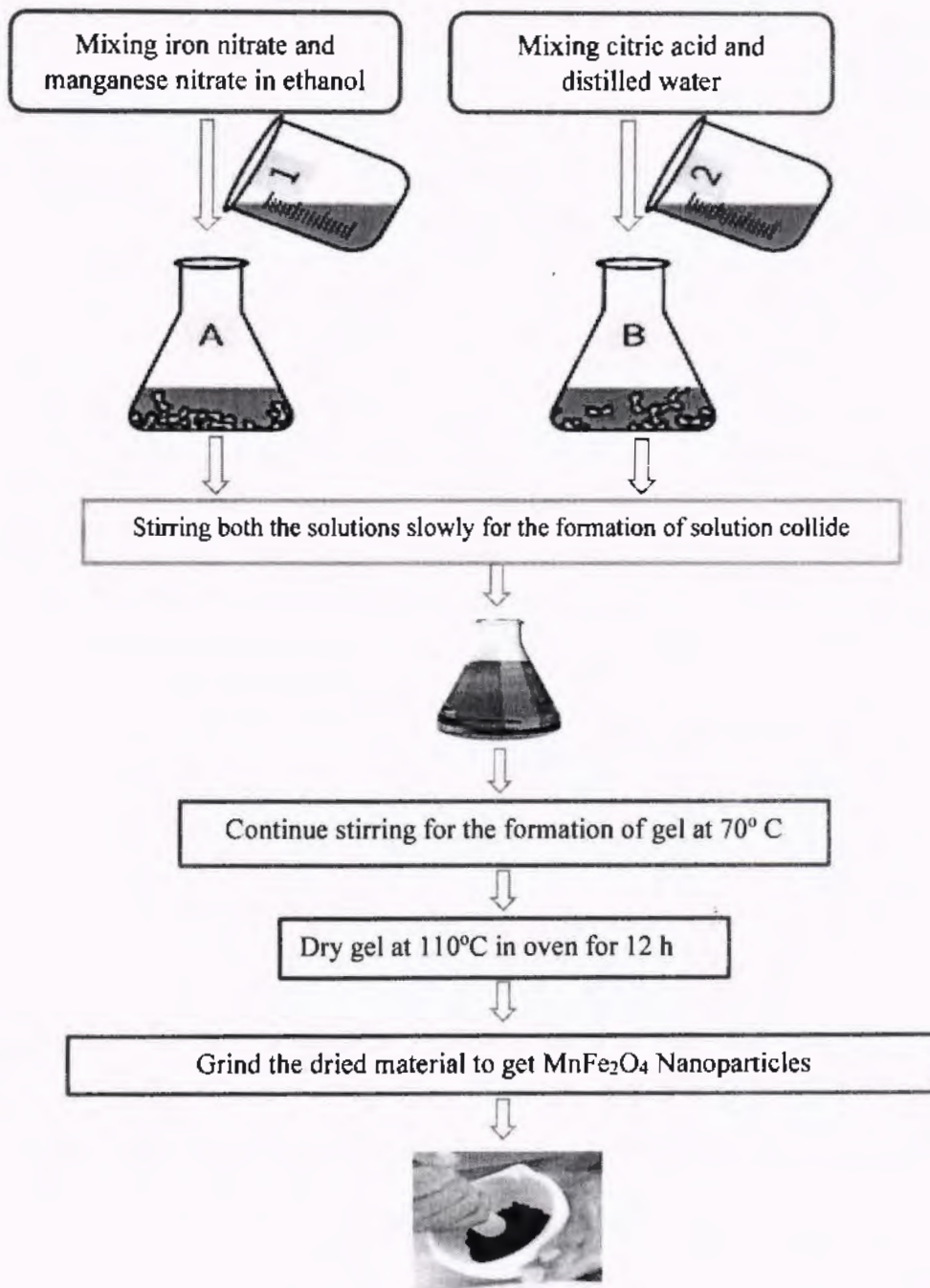


Fig. 3.2: schematic flowchart of sol-gel method for the synthesis of MnFe₂O₄ nanoparticles.

We prepared two solutions separately by mixing iron nitrate and manganese nitrate in ethanol and by mixing distilled water and citric acid, respectively. Now both the solutions were mixed slowly, and ammonia was added drop by drop with continuous stirring process to attain required PH level up to 5. Stirring the solutions constantly in oven for 70 °C temperatures to

form gel. Then drying gel at 110° C for 12 h in oven. Ground the dried material carefully for powder formation and annealed at 900° C for 2 h. The resultant material was again ground by means of agate motor and pestle to get fine powder of MnFe_2O_4 nanoparticles as end product.

3.3 Superconductor synthesis

For the preparation of high temperature superconductors different methods have been introduced. We used the most commonly well-known method for the preparation of CuTI-1223 superconductor is known as Solid State Reaction Method or Ceramic Method. By this method, during the preparation process the carriers concentration, the cation's configuration, oxygen stoichiometry, oxidation state of cation are the main factors necessary to be in command. This method depends upon the nature of the material, grinding, heating rate, homogeneous powder mixing, reaction temperature carbonates and metal oxides, and the duration of heat treatment nitrates are used as starting materials.

3.4 Synthesis of $\text{Cu}_{0.5}\text{Ba}_2\text{Ca}_2\text{Cu}_3\text{O}_{10-\delta}$ precursor

$(\text{MnFe}_2\text{O}_4)_x/\text{CuTI-1223}$ nanoparticles-superconductor composites were synthesized by Solid State reaction method. We took three compounds of $\text{Cu}_2(\text{CN})_2 \cdot \text{H}_2\text{O}$, $\text{Ca}(\text{NO}_3)_2$ and $\text{Ba}(\text{NO}_3)_2$ in amounts of 2.574gm, 3.524gm, and 3.902gm, respectively. These calculated amounts of given compounds were intermixed and placed in agate motor and pestle for grinding for at least 2 h. The grounded material was heated at 860°C upto 24 h by putting it in quartz boats. After 24 h we switched off the furnace to cool down the material. Repeat the same heating process with intermediate grinding for 1 h at least. We get the required precursor $\text{Cu}_{0.5}\text{Ba}_2\text{Ca}_2\text{Cu}_3\text{O}_{10-\delta}$ as shown in Fig. 3.3.

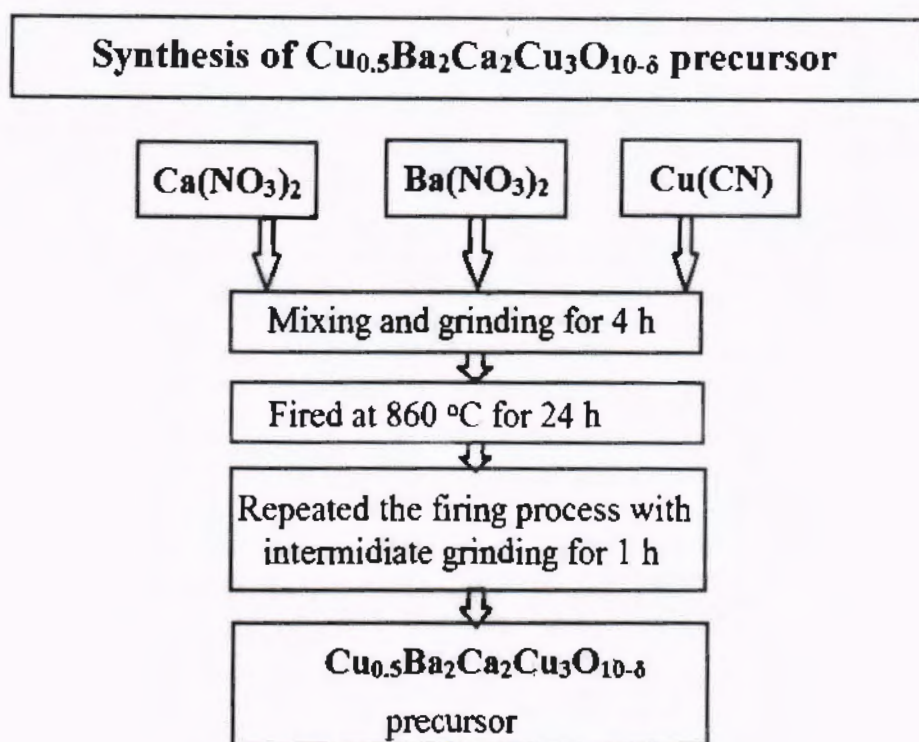


Fig. 3.3: diagram of preparation of precursor

3.5 Synthesis of $(\text{MnFe}_2\text{O}_4)_x/\text{CuTi-1223}$ nanoparticles-superconductor composite

Then we mixed 0.61 gm of Thallium oxide (Tl_2O_3) in a precursor along with MnFe_2O_4 nanoparticles with concentration of $x = 0, 0.5, 1.0, 1.5$ and 2.0 wt. % and grounded each sample for 1 h. After completing grinding we make pellets of the sample and for sintering we keep the pallet in gold capsule (due to non-reactive properties of Tl with Gold) and heated for 10 min at 860°C to get the required phase. In this way, we successfully synthesis $(\text{MnFe}_2\text{O}_4)_x/(\text{CuTi-1223})$ nanoparticles-superconductor matrix as shown in Fig. 3.4.



Fig. 3.4: complete flow diagram of preparation of $(\text{MnFe}_2\text{O}_4)_x/\text{Cu}_{0.5}\text{Tl}_{0.5}\text{Ba}_2\text{Ca}_2\text{Cu}_3\text{O}_{10.5}$ Nano-Superconductor.

3.6 Experimental techniques

Structural and phase purity of $(\text{MnFe}_2\text{O}_4)_x/(\text{CuTi-1223})$ nanoparticles-superconductor composites we used following characterization techniques. For structural analysis phase purity we used X-ray diffraction (XRD). Morphology was examined by SEM images. Resistance verses temperature measurements were done by four probe method. Impedance analysis in frequency ranges from 40 Hz to 100 MHz at various temperatures from 78 K to 253 K was investigated by LCR meter.

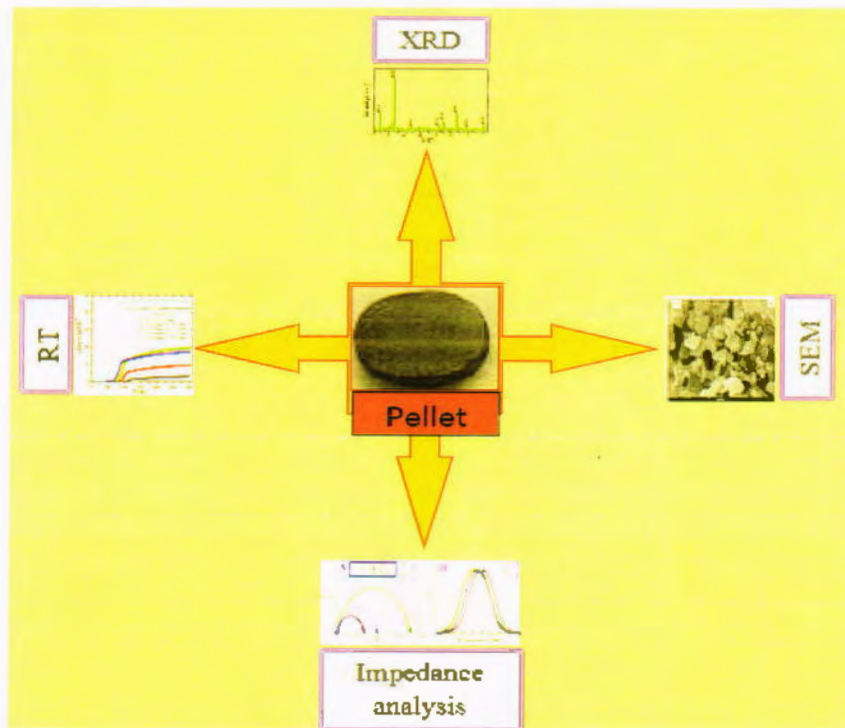


Fig. 3.5: Schematic diagram of characterization techniques of sample

3.6.1 XRD

The x-ray diffraction (XRD) is well-known powerful tool used to find out the nature of the given material whether the material is crystalline, amorphous or polycrystalline and also used to know the crystal size, crystal's orientation, their bonding, particle size, crystal shape and inter-planer spacing between the layers of atoms [32-33]. XRD spectra is also known as fingerprint of materials.

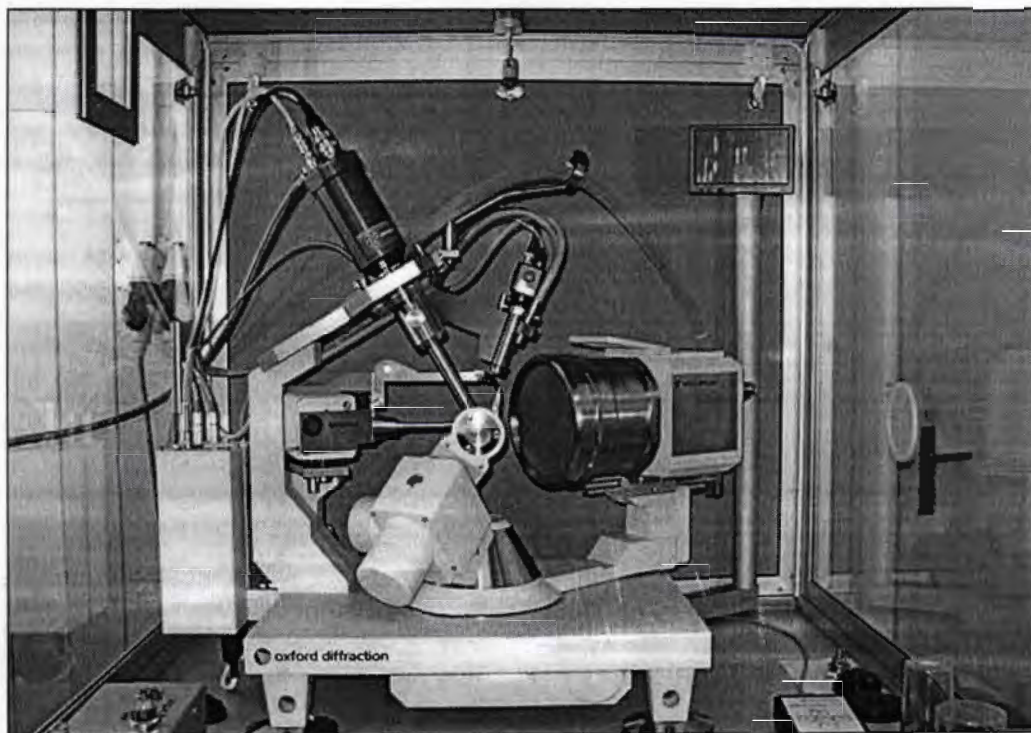


Fig. 3.6: Complete mechanism of XRD machine [33]

For the production of beam of electrons a cathode ray tube is used to heat the filament. A high voltage grid is applied to accelerate the electrons toward a target. These electrons are bombarded with target material which result in the production of X-rays of many components i.e. K_{α} and K_{β} . The detector rotated to record the x-ray pattern. The pattern of refracting x-ray based on the principle of Bragg's law. This X-ray signal is records and process by a detector and convert it into a count rate which finally plot on the screen of computer as an output.

3.6.1.1 Working principle

X-ray diffractometer work on the principle of Bragg's law. By the help of scattering angle of electrons, photons or neutrons, we can observe the crystal structure and inter-plane spacing. The pictorall representation of Bragg's law of x-rays as shown in Fig. 3.7.

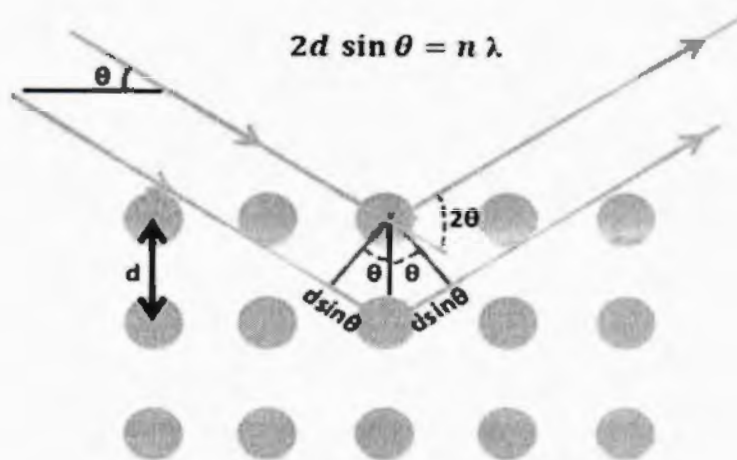


Fig. 3.7: Mechanism of Bragg's law [34]

One can identify the material structure after getting XRD pattern by comparing it with reference finger prints of materials. From spectrum the crystallite size of material can be calculated by Scherer formula:

$$D = 0.9\lambda / \beta \cos\theta \dots\dots\dots(3.1)$$

β represent FWHM, θ is Bragg's angle and D is average crystallite size [34].

3.6.1.2 Applications of XRD

- Structure of crystalline materials
- determination of lattice parameters of unit cell
- Measurements of purity of sample
- Textural measurements, i.e. the orientation of grains, fault in polycrystalline sample

3.6.2 Scanning electron microscopy (SEM)

Scanning electron microscope (SEM) is a kind of electron microscope that can be used for scanning the materials with the help of focused energetic beam of electrons to produce images. Electron gun used to emit beam of electrons, these focused beam of electrons generating many signals after the interacting with the atoms of sample [35]. The output signals then recorded by detectors to get the information of composition of the sample and the surface morphology.

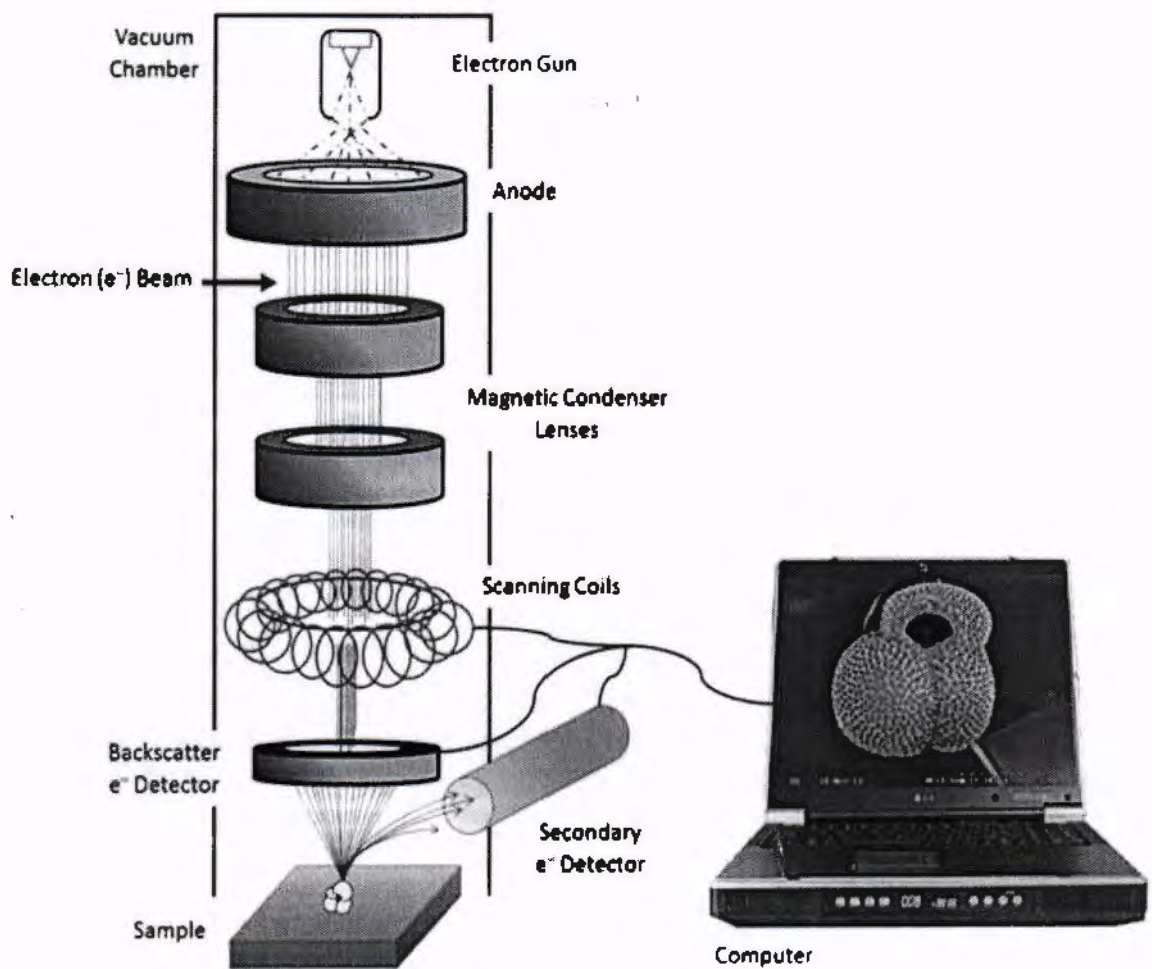


Fig.3.8: Schematic diagram of SEM setup [36].

3.6.2.1 Components of SEM

- **Electron Gun**

The electron gun is used for thermionic emission of fine beam of electron. These electrons then focused on the surface of the materials to detect their properties.

- **First Condenser lens**

The emitted electrons from target through thermionic emission are spread in all direction. The first condenser lens is used to focus the electron beams in one direction to the second condenser lens.

- **Second Condenser lens**

The second condenser lens are used adjust the size of the beam of electron impinging on the surface of the sample of material to be under investigation.

- **Deflection Coils**

For moving the scanning of the raster scan pattern an electromagnetic deflection coils are used for the deflection of the beam of electron.

- **Detectors**

The detectors or transducers are used to collect the back scattered electrons and secondary electrons [37].

3.6.3 Resistivity measurements by Four-probe method

To calculate the critical temperature 'T_c' of the superconductor (i.e. resistance is equal to zero, R=0) by using measure the resistivity of a superconductor. In normal state, the electrons scattering due to the defects in lattices, the vibrations of atoms in the lattice and the collisions between the electrons are the resistivity sources of the conducting materials.

The simple approach is used for the measurements of the resistivity in the conducting materials is the four-probe method. The surface of the rectangular shaped sample is connected by the four probes in this method. The low resistance contacts are normally used to connect the probes to the surface of the sample. The formula for the measurements of the resistivity is,

$$\rho = \frac{V(T)A}{IL}$$

Where, V(T) is the drop of the voltage across the surface of the sample. 'L' is the sample's length. 'I' is the current flow through the surface of the sample and 'A' is the sample's area of cross-section [38].

The current supply to the sample by a source of constant current across the outer probes and measure the voltage between the middle probes. During measurements applying a current of few milli-amperes (such as 1 or 2mA). The resistivity of temperature dependent is measured by using a liquid nitrogen dower which acts as a cryostat. During the cycle of heating such as 77K reaches to the room temperature, so we get the measurements of the resistivity. During the resistivity measurements applying the rate of heating from 1K/min to 3K/min. Now, the data is record by using the resistivity measurements setup as shown in figure.

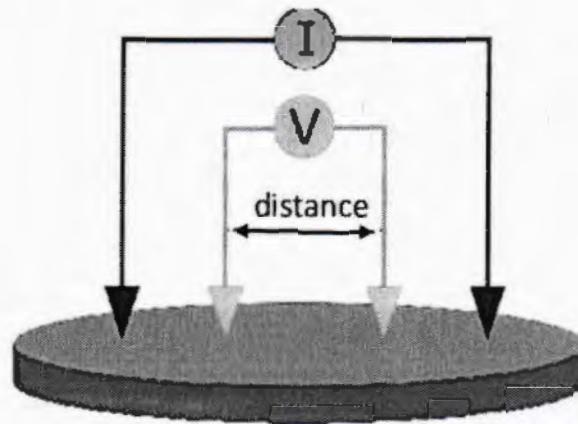


Fig. 3.9: Schematic diagram of four probe method [43].

3.6.4 Impedance analyzer

LCR meter is used to find the dielectric, impedance and modulus spectroscopy of materials. In our case, we used LCR meter for the impedance properties of CuTi-1223 matrix by the addition of MnFe_2O_4 nanoparticles with different concentrations. For impedance analyzer the following steps are involved to operate LCR meter [39].

In first step a conducting layers of silver paste were made on given samples to make connection between electrode and the sample. The sample act as insulator between these conducting layers of silver paste. Placed the sample in holder to make connection between conducting layers with the sample holder. The conducting layers are connected to wires and then connect with LCR meter. On the other hand, thermocouple is connected to the P-2000/E KEITHLEY MULTIMETER. Thermocouple is used to find the temperature which is function of voltage. A thermocouple then placed in liquid nitrogen to decrease the temperature up to 78 K. In this way impedance parameters are tuned at various temperatures and frequency ranges by recording values on LCR meter.

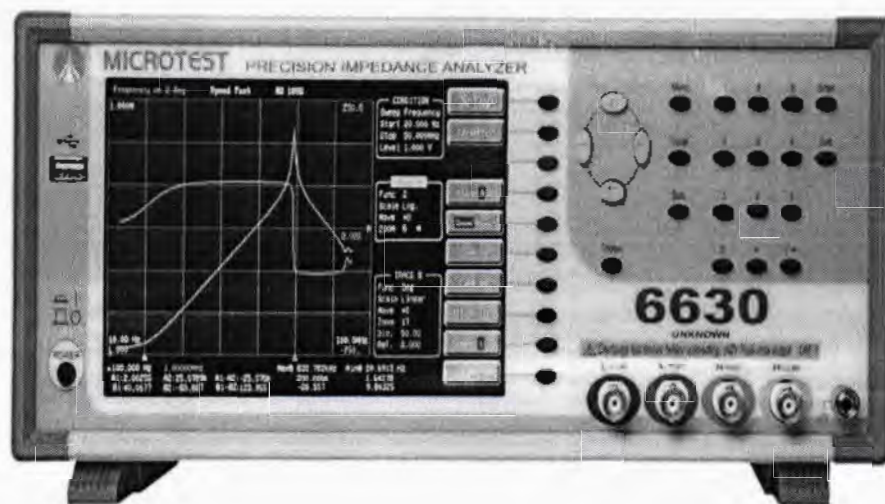


Fig. 3.10: Impedance analyser (LCR meter) [40]

Chapter 4: Results and Discussion

4.1 X-Ray diffraction analysis (XRD)

For the crystal structure and phase purity of material we used XRD technique. In the inset of Fig. 4.1 the XRD spectrum of MnFe_2O_4 nanoparticles is shown. Various planes like (2 2 0), (3 1 1), (4 0 0), (5 1 1), and (4 4 0) are indexed according to the cubic structure corresponding to different $2\theta^\circ$ values [41]. We used Scherer's formula to find particle size, which is found to be 20 nm. All obtained peaks are fully matched with finger prints of cubic crystal structure of MnFe_2O_4 nanoparticles and no significant impurity peaks of high intensity was observed.

Representative XRD spectra of $(\text{MnFe}_2\text{O}_4)_x/\text{CuTi-1223}$ nanoparticles-superconductor for $x = 0$ and 2.0 wt.% are shown in Fig. 4.1. These diffraction planes clearly showed about the phase purity of CuTi-1223 superconducting matrix. By following $p4/mmm$ space group we found from XRD spectra that all the major peaks are well matched with the tetragonal structure of host matrix. By the addition of these MnFe_2O_4 nanoparticles no prominent alteration in XRD spectrum of this phase was observed. Some small peaks without indexing were observed in the pattern may be due to some other phases and impurity

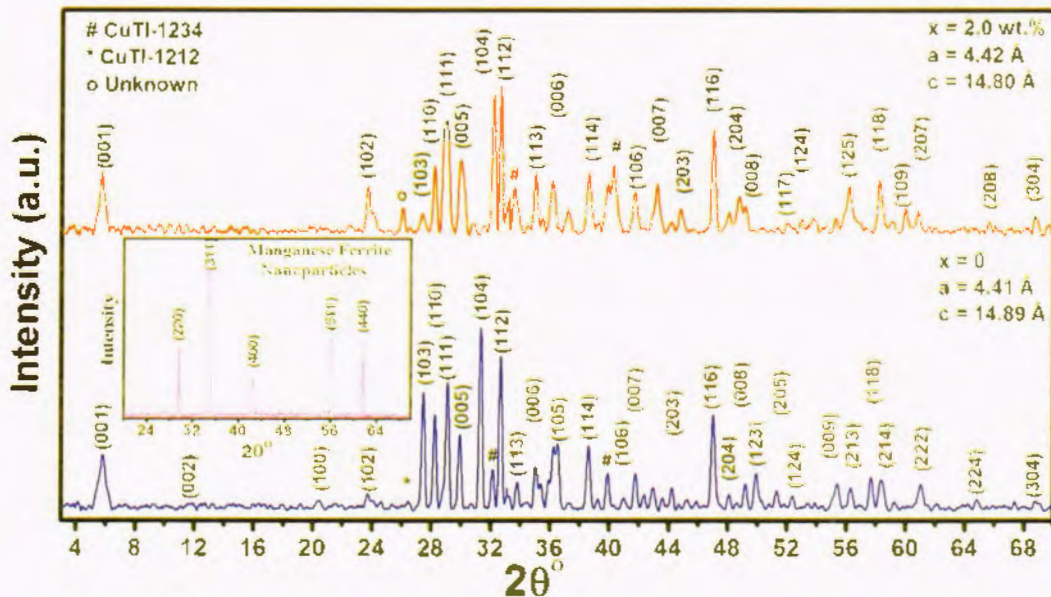


Fig. 4.1: XRD of $(\text{MnFe}_2\text{O}_4)_x/\text{CuTi-1223}$ composite with ($x = 0$ and 2.0 wt.%) and XRD of MnFe_2O_4 nanoparticles is shown in the inset.

4.2 SEM analysis

For structure analysis like morphology and surface features we used scanning electron microscopy (SEM). In the inset of Fig. 4.2 SEM images of $(\text{MnFe}_2\text{O}_4)_x/\text{CuTi-1223}$ composites was shown for $x = 0, 2.0$ wt.%. The micrographs of SEM for $x = 0$ % shows higher density of pores and voids and weak-links. But for $x = 2.0$ wt.% inclusion of these nanoparticles in bulk CuTi-1223 matrix the empty gaps are healed up and voids are improved. These MnFe_2O_4 nanoparticles changes the morphology of grains in a material due to the change of thermodynamics of reaction.

4.3 dc resistivity measurements (RT)

The dc resistivity (R-T) measurements of $(\text{MnFe}_2\text{O}_4)_x/\text{CuTi-1223}$ nanoparticles-superconductor for $x = 0$ and 2 wt.% is shown in Fig. 4.2. In (HTSCs) there are two types of critical temperatures for resistivity i.e. T_c^{onset} (K) and the other is $T_c(0)$. The electronic properties of materials depend upon T_c^{onset} (K) while micro-structure properties of materials are related to the value of $T_c(0)$. The value of T_c^{onset} (K) was found to be 94 K for un-added pure CUTI-1223 sample, which was decreased to 92 K for $x = 2.0$ wt.% addition of MnFe_2O_4 nanoparticles. These suppress in superconducting properties with the inclusion of MnFe_2O_4 nanoparticles in bulk CuTi-1223 matrix is due to the magnetic natured nanoparticles. The enhanced the charge accumulation at grain-boundaries has reduced the mobility of charge carriers in the material. Normal state resistivity showed non-monotonic variation with addition of MnFe_2O_4 nanoparticles inclusion in host CuTi-1223 phase, which is due to the irregular distribution of nanoparticles [42].

TH: 18380

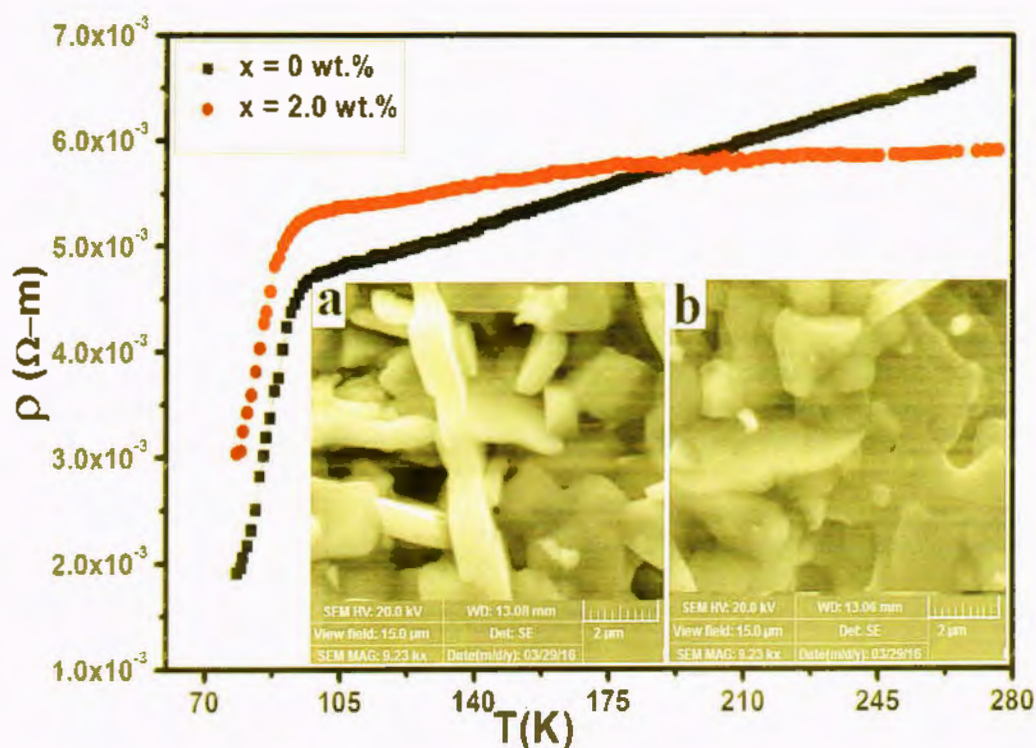


Fig. 4.2: R-T measurements of $(\text{MnFe}_2\text{O}_4)_x/\text{CuTi-1223}$ composite for $x = 0$ and 2.0 wt.%, and the SEM images of $(\text{MnFe}_2\text{O}_4)_x/\text{CuTi-1223}$ composites with (a) $x = 0$ and (b) 2.0 wt. % is shown in the inset.

4.4 Impedance analysis

Complex impedance analysis has been used to correlate the ac-electrical properties with the microstructure of material. We have studied the impedance properties of $(\text{MnFe}_2\text{O}_4)_x/\text{CuTi-1223}$ composites. The electrical behavior of ferrites and cuprates can be understood in detail with the help of some theoretical models. By Koop's model the two layers of cuprates and ferrites are considered one is grains (conducting region) and other is grain-boundaries (non-conducting region). Therefore grain-boundaries more chemically reactive as compare to grains, and often impurity atoms segregate along these grain-boundaries due to their higher energy state. [43]. The flow of charge carriers have to face hurdle to flow from conducting layer to non-conducting layer [44]. To understand this, we can modelled an equivalent circuit consist of grain resistance ' R_g ' connected in series with grain-boundaries resistance ' R_{gb} ' parallel with grain-boundaries capacitance ' C_{gb} ' as shown in Fig. 4.3.

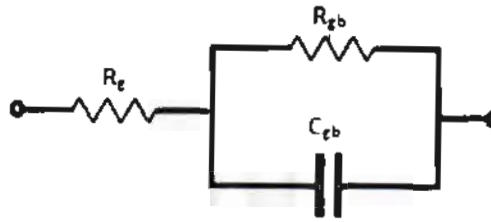


Fig. 4.3: The electrical equivalent circuit for impedance.

4.4.1 Nyquist Plot

The representative Nyquist plots of $(\text{MnFe}_2\text{O}_4)_x/\text{CuTi-1223}$ ($x = 0, 1.0$ and 2.0 wt.%) composites at temperatures from 78 K to 253 K, in frequency ranges from 40 Hz to 10 MHz are shown in Fig. 4.4 (a-c). We observed that the diameters of semicircles get depressed with the increase of temperature, which indicated the non-Debye type relaxation phenomenon in the material. From these semi-circles, we can find the value of ' R_g ' and ' R_{gb} '. The left intercept of the semicircle with Z' -axis gives ' R_g ' value and the right one gives the total resistance $R = R_{gb} + R_g$. From Nyquist plot it was found that the ' R_{gb} ' values are greater than ' R_g ', which proves that the grain-boundaries are more resistive than grains. This is probably due to the non-stoichiometric distribution of oxygen, spin-charge reflection and dangling bonds on the grain-boundaries [45]. By the addition of MnFe_2O_4 nanoparticles in CuTi-1223 matrix, it is found that the total resistance has been increased from 2.0×10^3 to 9.7×10^5 for $x = 0$ to 2.0 wt. % at 78 K temperature, which is due to the magnetic nature of these nanoparticles. The charge accumulation has been enhanced at grain-boundaries, which causes the reduction of flow of charge carriers. This band spread of Z' (Ω) versus Z'' (Ω) with the addition of MnFe_2O_4 nanoparticles clearly indicate that the dielectric response of the material has been improved. We found that by increasing temperature from 78 K to 253 K, the total resistance of $(\text{MnFe}_2\text{O}_4)_x/\text{CuTi-1223}$ matrix were decreased from 2.0×10^3 to 1.6×10^3 , 5.4×10^4 to 3.7×10^4 and 9.7×10^5 to 6.0×10^4 for $x = 0, 1.0$, and 2.0 wt.% respectively, which is probably due to release of space charges at grain-boundaries by increasing temperatures. It means that by increasing temperatures from superconducting state to normal state the total resistance has been decreased for all the samples.

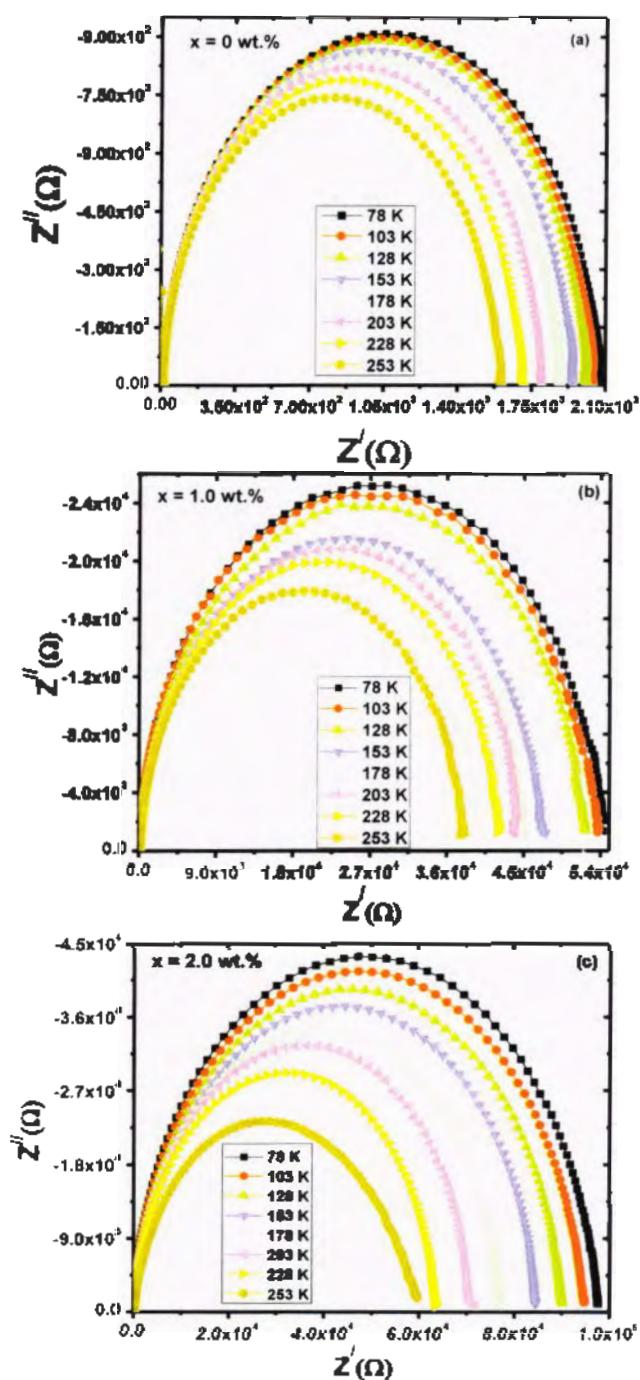


FIG. 4.4(a-c): The Nyquist plot of impedance between real part (Z') and imaginary part (Z'') for $(\text{MnFe}_2\text{O}_4)_x/\text{CuTi-1223}$ with (a) $x = 0$ at $T = 78 \text{ K}$ to 253 K , (b) $x = 1.0 \text{ wt.}\%$ at $T = 78 \text{ K}$ to 253 K , (c) $x = 2.0 \text{ wt.}\%$ at $T = 78 \text{ K}$ to 253 K .

4.4.2 Activation Energy Calculation

The activation energy of grains and grain-boundaries were calculated by applying small polaron hopping model (SPH);

$$\frac{R}{T} = A_0 e^{\frac{E_c}{kT}} \quad \text{----- (1)}$$

Where A_0 is constant, R and T are resistance and temperature, E_c is activation energy of conduction and k is the Boltzmann constant. From the slopes of fitted straight lines, the calculated activation energies of grains and grain-boundaries for $(\text{MnFe}_2\text{O}_4)_x/\text{CuTi-1223}$ composites with $x = 0$ and 2 wt.% are shown in Fig. 4.5 (a, b). The calculated activation energy for conduction on grains was found to be 0.215 meV, 0.2158 meV and 0.216 meV, and for grain-boundaries was 0.207 eV, 5.18 eV and 10.6 eV for $x = 0, 1.0$ and 2 wt.%, respectively. The higher value of activation energy at grain-boundaries clearly shows that the resistive property is more prominent at grain-boundaries than grains [46] We found the activation energy of grain-boundaries for $(\text{MnFe}_2\text{O}_4)_x/\text{CuTi-1223}$ nanoparticle-superconductor composite with $x = 0, 1.0$ and 2.0 wt. % is about 0.207 eV, 5.18eV and 10.6 eV respectively, which is a linear trend in increase of activation energy against added nanoparticles wt. %. The increase in activation energy can be explained in term of cooper pair's breakdown, which may be attributed to spin-charge reflection and trapping of charge carriers due to presence of magnetic nanoparticles at grain-boundaries of CuTi-1223 phase. These magnetic impurities tend to localize onsite charges and suppress the tunneling of carriers between grain and grain-boundaries which result in insulating behavior. High tendency of oxygen vacancies may also cause such increase in activation energy [47]. High tendency of oxygen vacancies may also cause such increase in activation energy.

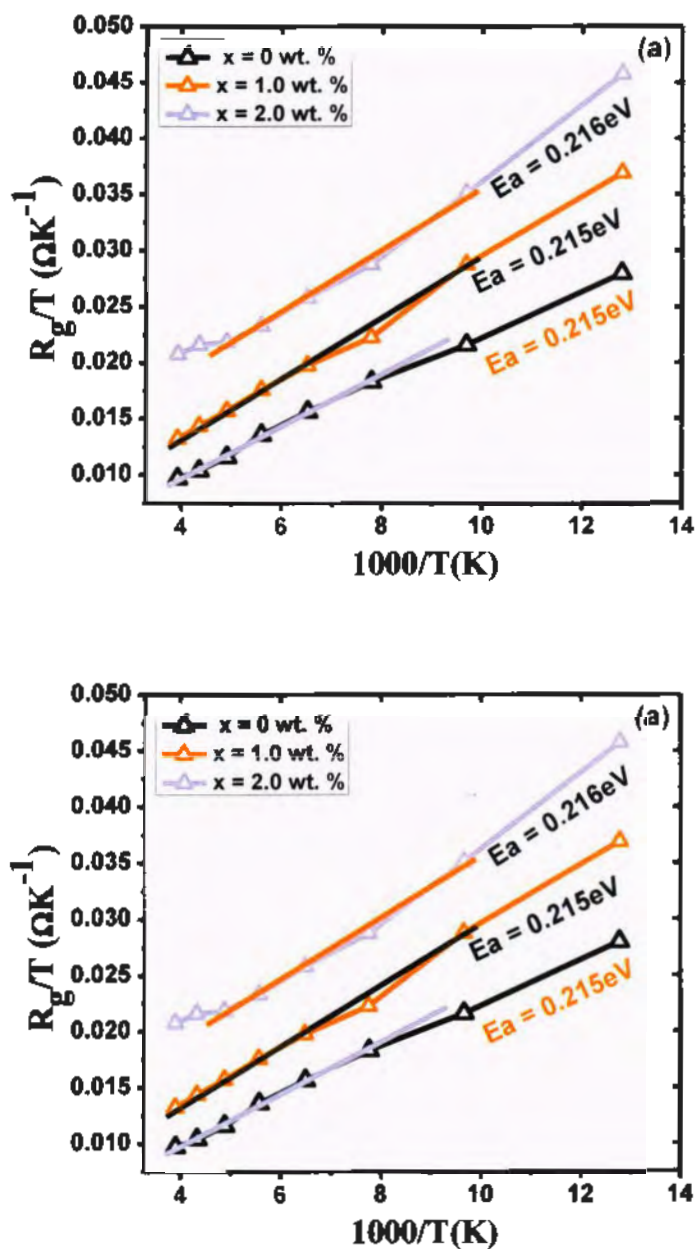


Fig. 4.5(a, b): (a). The plots of R_{gb}/T versus $1000/T$ for $x = 0, 1.0$ and 2.0 wt%. (b). The plots of R_{gb}/T versus $1000/T$ for 1.0 wt. % and $x = 2.0$ wt.%. In the inset of (b) for $x = 0$ %.

4.4.3 Real Part of Impedance

To understand the conduction mechanism and dynamic of mobility, we plotted frequency dependent real part of impedance Z' at various temperatures from 78 K to 253 K as shown in Fig. 4.6 (a-c). The variation of Z' versus operating temperatures T (K) at 40 Hz frequency indicating the gradual decrease in Z' with increasing the value of temperature are shown in the insets of Fig. 4.6 (a-c). The maximum value of Z' at frequency of 40 Hz and at low temperature (78 K) were found to be 2.07×10^3 , 5.4×10^4 , 9.8×10^4 , for the samples with $x = 0$, 1.0 and 2.0 wt. %, respectively. At low frequencies the value of $Z'(\Omega)$ jump to high value, this is because at low frequency, the charges at interface trap can easily follow the applied ac electric field and yield an excess capacitance, which depends on the frequency and time constant of interface states [47]. It is observed that the magnitude of $Z'(\Omega)$ is more pronounced after the inclusion of MnFe_2O_4 nanoparticles in CuTi-1223 phase, which is due to the magnetic nature of these nanoparticles. The nanoparticles were settled at grain-boundaries and enhance the interface polarization mechanism which result the decrease in ac-conductivity of composite. The maximum value of Z' at frequency of 40 Hz varied from 2.07×10^3 to 1.6×10^3 , 5.4×10^4 to 3.8×10^4 , 9.8×10^4 to 6.0×10^4 at 78 to 253 K for the samples with $x = 0$, 1.0 and 2.0 wt. %, respectively. Initially, the value of Z' decreases with frequency and temperature for all the samples, this may be due to the slow dynamic of mobility. At higher frequency Z' merge regardless of temperature, this is due to the release of space charges at grain-boundaries as a result of reduction in the barrier properties of material with the increase of temperature [48-50].

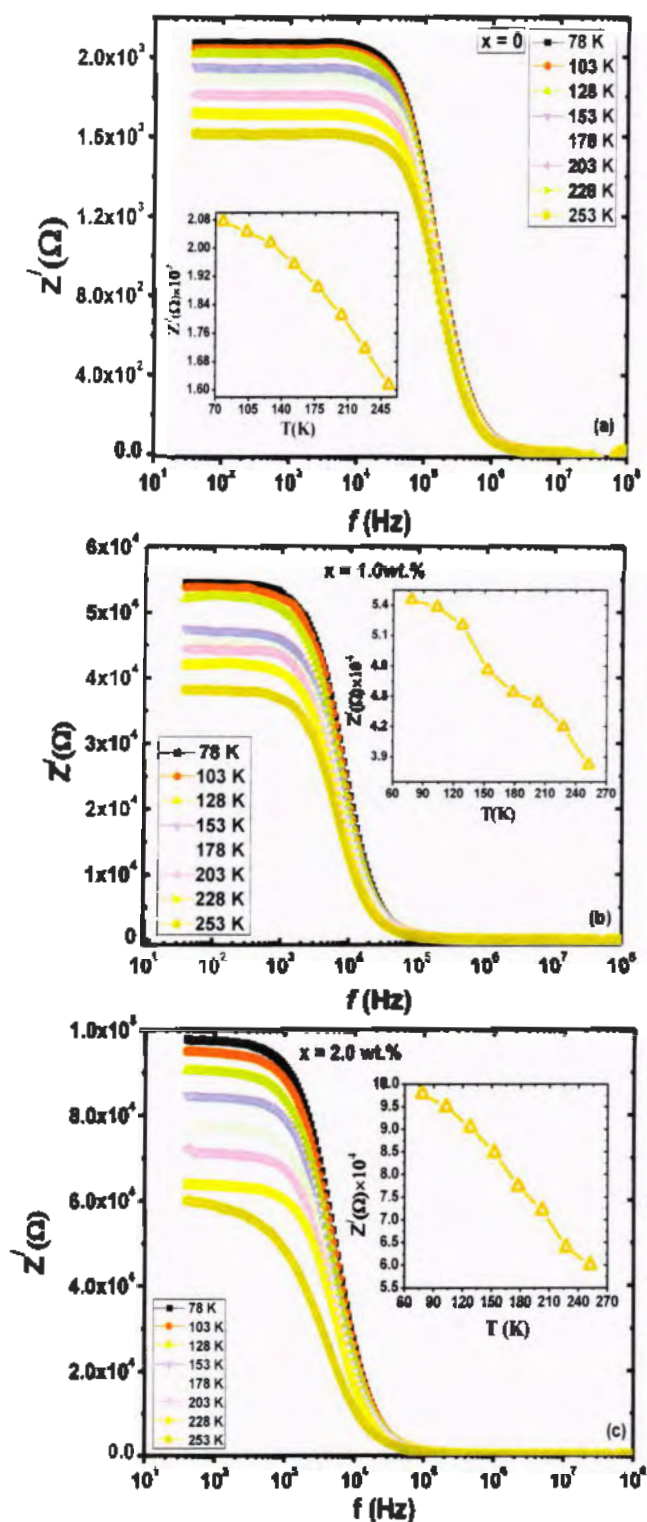


Fig. 4.6 (a-c): Variation of impedance real part (Z') versus frequency (40 Hz- 10 MHz) for $(\text{MnFe}_2\text{O}_4)/\text{CuTi-1223}$ for $x = 0, 1.0$ and 2.0 wt.% with temperatures from 78 K to 253 K and the variation of Z' versus T from (78 K to 253 K) at frequency of 40 Hz are shown in the insets.

4.4.4 Imaginary Part of Impedance

To understand the relaxation process within crystallite grains and grain-boundaries, we plotted graphs between imaginary part (Z'') and test frequency from 40 Hz to 10 MHz for various temperatures from 78 K to 253 K as shown in Fig. 4.7 (a-c). The curves indicate that Z'' reaches at peak (Z''_{\max}) for all temperatures and the maximum values of Z''_{\max} were found to be -9.1×10^2 , -2.5×10^4 , -4.3×10^4 at low temperature (78 K) for $x = 0$, 1.0 and 2.0 wt. % samples, respectively. In the inset of Fig. 4.7(a-c), there shown a variation of Z''_{\max} versus temperature, which indicated that the value of Z''_{\max} decreases by the increase of temperature. This is due to the release of space charges present at grain-boundaries. This decrease in Z''_{\max} with temperature is a factor responsible for the increase of conductivity of material. With the increase in concentration of added these MnFe_2O_4 nanoparticles in host CuTi-1223 phase, the magnitude of Z''_{\max} were increased, due to the magnetic nature of these nanoparticles interaction with mobile carriers at grain-boundaries [51]. The maximum value of Z''_{\max} varied from -9.1×10^2 to -7.3×10^2 , -2.5×10^4 to -1.8×10^4 , -4.3×10^4 to -2.5×10^4 at temperatures from 78 to 253 K with $x = 0$, 1.0 and 2.0 wt. % samples, respectively. The curves indicate that by adding these MnFe_2O_4 nanoparticles in bulk CuTi-1223 matrix, the peak positions of Z''_{\max} shifted towards lower frequency. This is because the nanoparticles are settled at grain-boundaries, which enhance the charge accumulation at grain-boundaries and suppress the tunneling of electrons between grain and grain-boundaries. Now the grain-boundaries offered more resistance ' R_{gb} ' and capacitance ' C_{gb} '. The shifting of peak positions of Z''_{\max} towards lower frequency can be understand by this increase of ' R_{gb} ' and capacitance ' C_{gb} ' according to;

$$\omega = 2\pi f = \frac{1}{\tau} = \frac{1}{C_{gb}R_{gb}} \quad \text{----- (2)}$$

By increasing ' R_{gb} ' and ' C_{gb} ', the relaxation time (τ) increases, this causes the shifted of peaks to lower frequency. The shifting of these peaks towards the lower frequency arises losses in the materials witnessed the decrease in ac-conductivity by increasing concentration of MnFe_2O_4 nanoparticles.

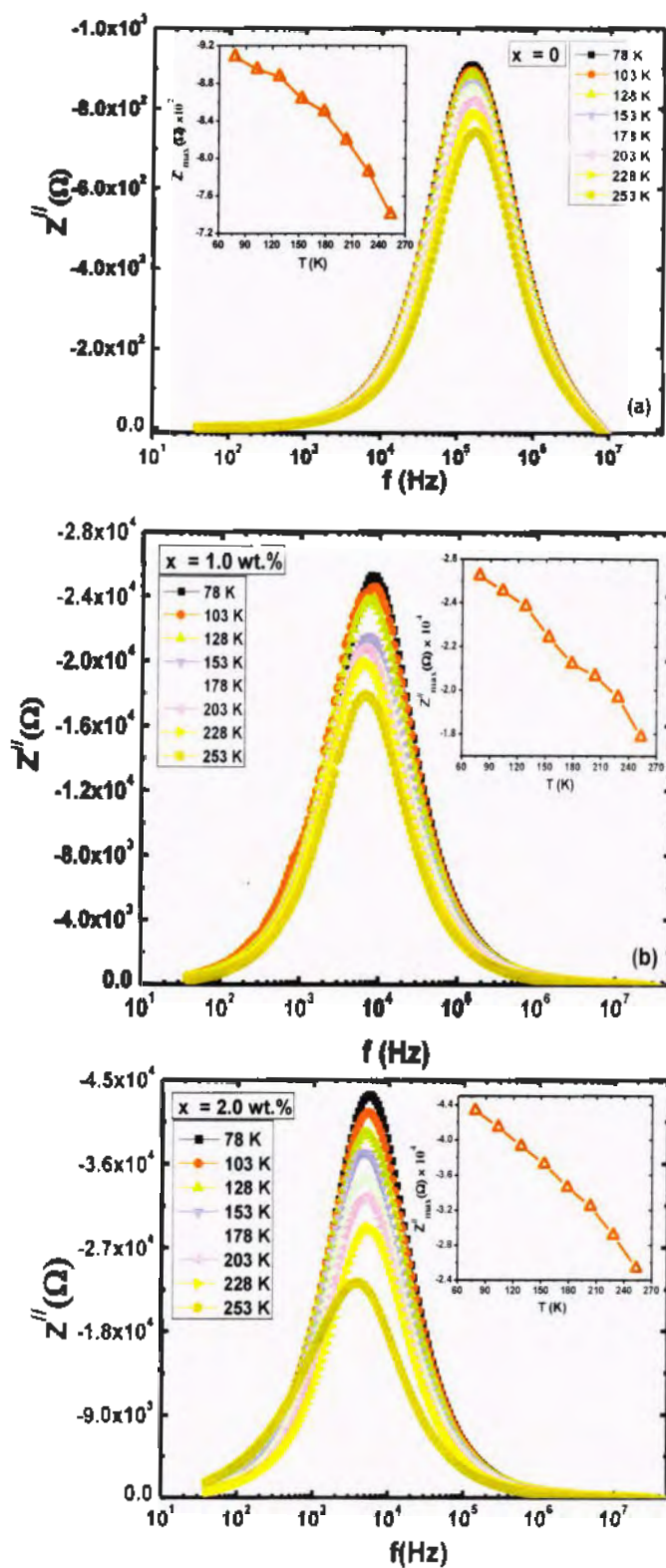


Fig. 4.7(a-c): Variation in imaginary part (Z'') versus frequency (40Hz- 10MHz) for $(\text{MnFe}_2\text{O}_4)_x/\text{CuTi-1223}$ composite for $x = 0, 1.0$ and 2.0 wt.% with $T = 78 \text{ K}$ to 253 K and the variation of Z''_{max} versus T ($78 \text{ K} - 253 \text{ K}$) are shown in the insets.

4.4.5 Non-Debye type relaxation phenomenon

The dielectric relaxation time is an important parameter to understand the conduction mechanism in materials. In Debye relaxation process all dipoles in the system relax with the same relaxation time (single relaxation time approximation). Ideal Debye relaxation has no practical application except in liquids and perfect crystal. But real materials usually exhibit broad relaxation time distribution and can be characterized by a pre-exponential factor. The non-Debye type relaxation phenomenon can be understood by following relation;

$$\phi(t) = e^{-\left(\frac{t}{\tau}\right)^\beta} \quad \text{with} \quad 0 < \beta < 1 \quad \text{-----} \quad (3)$$

Where $\phi(t)$ is the time evolution of an electric field within the composites, τ is the relaxation time and β is Kohlrausch parameter, which can be calculated by the relation $\beta = 1.14/\text{FWHM}$. We plotted an impedance master curves at various temperatures for $(\text{MnFe}_2\text{O}_4)_x/\text{CuTi-1223}$ composites with $x = 0, 1.0$ and 2.0 wt.% between normalized parameters Z''/Z''_{max} and f/f_{max} to confirm, whether the distribution of relaxation time is temperature dependent or not, as shown in Fig. 4.8(a-c). The coincidence of all curves into one master curves at operating temperatures indicate that the distribution of dynamic process (relaxation time) is almost temperature independent and non-exponential type of conduction process. The value of full width at half maximum abbreviated as (FWHM) for $x = 0, 1.0$ and 2.0 wt. % are found to be greater than 1.14 decades (ideal Debye characteristics $\beta = 1$), causes the smaller value of β , which is found to be less than one for all the samples. This is the confirmation of deviation from Debye-type relaxation. These outcomes suggest that the ions migration takes place through hopping mechanism [53-54].

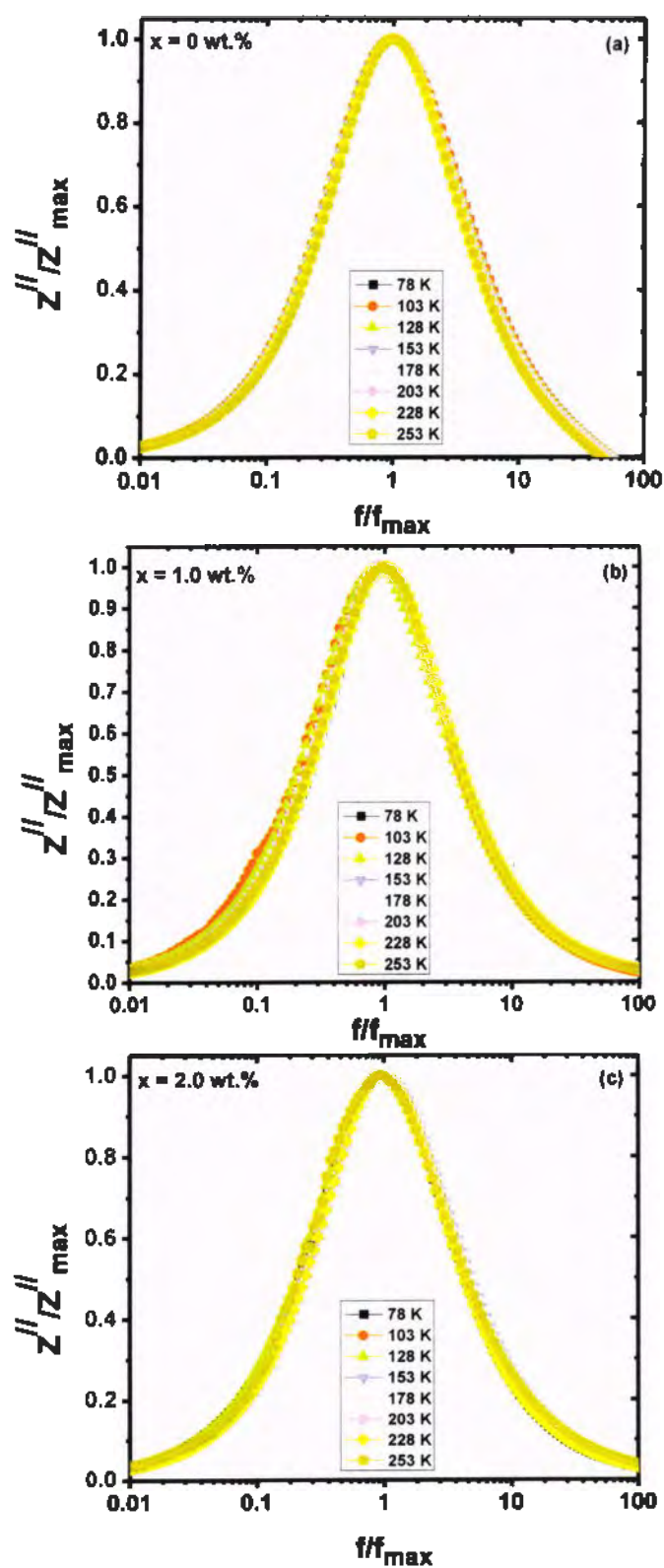


Fig. 4.8 (a-c): The master curves of normalized parameters Z''/Z''_{\max} versus f/f_{\max} for $(\text{MnFe}_2\text{O}_4)_x/\text{CuTi-1223}$ composite with $x = 0, 1.0$ wt.% and 2.0 wt.% at $T = 78$ K to 253 K

4.4.6 ac-conductivity (σ_{ac})

The ac-conductivity (σ_{ac}) of $(\text{MnFe}_2\text{O}_4)_x/\text{CuTi-1223}$ ($x = 0, 1, \text{ and } 2 \text{ wt.}\%$) nanoparticles-superconductor composites at various temperatures from 78 K to 253 K by varying applied frequency are shown in Fig. 4.9 (a-c). The value of σ_{ac} at lower frequency of 40 Hz were found around 6.6×10^{-6} , 2.04×10^{-7} , 1.05×10^{-7} at 78 K temperature for $x = 0, 1.0$, and 2.0 wt. % samples, respectively. This decrease in σ_{ac} with increasing concentration of added these MnFe_2O_4 nanoparticles, clearly the result formation of space charges by magnetic interaction of these MnFe_2O_4 nanoparticles with charge carriers at grain-boundaries as mention above. In the insets of Fig. 4.9 (a-c), the variation of σ_{ac} versus operating temperatures at low frequency of 40 Hz is shown. The value of σ_{ac} at lower frequency of 40 Hz varied from 6.7×10^{-6} to 8.67×10^{-6} , 2.04×10^{-7} to 3.3×10^{-7} and 1.05×10^{-7} to 1.7×10^{-7} at temperatures 78 K to 253 K for $x = 0, 1.0$ and 2.0 wt. % samples, respectively. This is attributed to the gradual increase in σ_{ac} with increasing value of operating temperatures, which enhances hopping rate of mobile charge carriers [55-56].

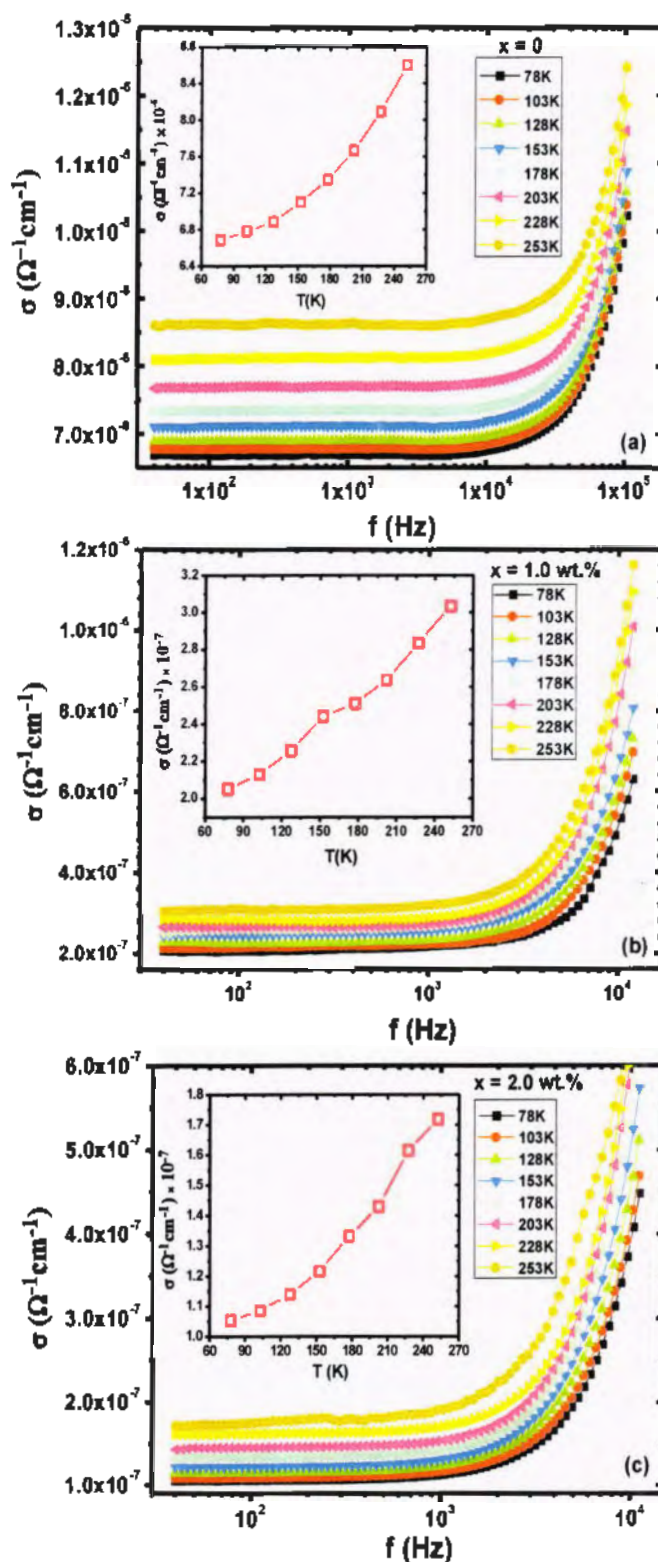


Fig. 4.9(a-c): ac-conductivity (σ_{ac}) versus frequency for $(\text{MnFe}_2\text{O}_4)_x/\text{CuTi-I223}$ with (a) $x = 0$, 1.0 and 2.0 wt.% for 78 K to 253 K operating temperature. variation in σ_{ac} versus operating temperature at frequency of 40 Hz is shown in the insets.

Conclusion

CuTi-1223 superconducting phase has been prepared by solid state reaction method. To tune the conduction mechanism and electrical properties we add the concentration of MnFe_2O_4 nanoparticles with $x = 0, 1.0$ and 2.0 wt.% in this phase. No phase alteration was observed in XRD spectra by adding MnFe_2O_4 nanoparticles. Empty spaces and pores are improved as confirmed by SEM micrographs. Superconducting phase (T_c) were decreased with the increase of MnFe_2O_4 nanoparticles content in CuTi-1223 matrix due to pair breaking mechanism as a result of spin-charge reflection due to presence of these nanoparticles at grain-boundaries of CuTi-1223 phase. Temperature and frequency dependence of complex impedance has shown the non-Debye type relaxation in this material. The broadness of Nyquist plot of Z' versus Z'' with the addition of MnFe_2O_4 nanoparticles is due to the enhancement of the interface polarization mechanism. Complex impedance plots revealed that the grain-boundaries are more resistive than grains. The MnFe_2O_4 nanoparticles suppress the tunneling of electrons between grain and grain-boundaries which result in increasing activation energy. The impedance master curves indicated that the distribution of relaxation time (dynamic process) was nearly temperature independent. The decrease in ac-conductivity with increasing contents of these nanoparticles indicated the enhancement of space charges at grain-boundaries.

Bibliography:

- [1] Loveday, David, P. Peterson, and Bob Rodgers, "Evaluation of organic coatings with electrochemical impedance spectroscopy" "Application of EIS to coatings", *JCT coatingstech* **1**, 88(2004).
- [2] Wagner, Norbert, and K. A. Friedrich, "Application of electrochemical impedance spectroscopy for fuel cell characterization", *Fuel Cells* **9**, 237(2009).
- [3] P. Agarwal, M. E. Orazem, and L. H. Garcia-Rubio, "Measurement models for electrochemical impedance spectroscopy and Demonstration of applicability", *J. Electrochem. Soc.* **139**, 1917(1992).
- [4] M. Donald and J. Ross, "Impedance Spectroscopy, Emphasizing Solid Materials and Systems", John Wiley & Sons, (1987).
- [5] E. Barsoukov and, J. R. Macdonald, "Impedance spectroscopy, theory, experiment, and applications", John Wiley & Sons, (2005).
- [6] P. Wood, D. C. Sinclair, and F. P. Glasser, "Electrical characterisation of bismuth orthovanadate using ac impedance spectroscopy", *Solid state ionics* **66**, 151(1993).
- [7] M. R. H. Khan and M. Saji, "Comparative study of admittance spectroscopy and DLTS in determining trap levels of CdTe-ZnTe heterojunctions" *Solid-State Electron.* **29**, 253(1986).
- [8] S. P. Yadav, S. S. Shinde, A.A. Kadam, and K.Y. Rajpure, "Structural, morphological, dielectric, magnetic and impedance properties of $\text{Co}_{1-x}\text{Mn}_x\text{Fe}_2\text{O}_4$ ", *J. Alloys Compd.* **555**, 330(2013).
- [9] K. Chabowski, A. F. Junka, P. Szymczyk, T. Piasecki, A. Sierakowski, B. Maczynska and K. Nitsch, "The Application of Impedance Microsensors for Real-Time Analysis of *Pseudomonas aeruginosa* Biofilm Formation" *Pol. J. Microbiol.* **64**, 115(2015).
- [10] D. A. Bonn, S. Kamal, A. Bonakdarpour, R. Liang, W. N. Hardy, C. C. Homes, D. N. Basov, and T. Timusk. "Surface impedance studies of YBCO", *Czech. J. Phys.* **46**, 3195(1996).
- [11] K. Prasad, A. Kumar, S. N. Choudhary, and R. N. P. Choudhary, "relaxor behavior of $\text{Pb}[(\text{Mg}_{2/3}\text{Co}_{1/3})_{1-\beta}\text{Nb}_{2/3}]\text{O}_3$ ceramic", *solid state ionics* **176**, 1641(2005).
- [12] J. Li, F. Li, C. Li, G. Yang, Z. Xu, and S. Zhang "Evidences of grain-boundary capacitance effect on the colossal dielectric permittivity in (Nb + In) Co-doped TiO_2 ceramics", *Royal Soc. Chem. Adv.* **5**, 8295 (2015).

- [13] B. Behera, P. Nayak, R.N.P. Choudhary, "Impedance spectroscopy study of $\text{NaBa}_2\text{V}_5\text{O}_{15}$ ceramic", *J. Alloy compd.* **436**, 226(2007).
- [14] G. Liu, H. Fan, Z. Liu, and Y. Zhao, "Colossal permittivity and impedance analysis of niobium and aluminum co-doped TiO_2 ceramics", *Soc. Chem. Adv.* **54**, 48708(2016).
- [15] P. S. Sahoo, B. B. Mohanty, M. P. K. Sahoo, R. N. P. Choudhary, and Ram "Impedance Spectroscopy of $\text{Ba}_5\text{GdTi}_3\text{V}_7\text{O}_{30}$ ", *J. Phys. Mod.* **5**, 357(2012).
- [16] N. K. Singh, P. Kumar, B. P. Singh, and T. P. Sinha, "Dielectric and impedance properties of $\text{Sr}(\text{Sm}_{0.5}\text{Nb}_{0.5})\text{O}_3$ ceramics", *Solid State Science* **13**, 2060(2011).
- [17] S. P. Yadav, S. S. Shinde, A.A. Kadam, and K.Y. Rajpure, "Structural, morphological, dielectrical, magnetic and impedance properties of $\text{Co}_{1-x}\text{Mn}_x\text{Fe}_2\text{O}_4$ ", *J. Alloys Compd.* **555**, 330 (2013)
- [18] Lily, K. Kumari, K. Prasad, and R. N. P. Choudhary, "Impedance spectroscopy of $(\text{Na}_{0.5}\text{Bi}_{0.5})(\text{Zr}_{0.25}\text{Ti}_{0.75})\text{O}_3$ lead free ceramic", *J. Alloys Compd.* **453**, 325 (2008).
- [19] N. H. Mohammed, "Effect of MgO Nano-oxide Additions on the Superconductivity and Dielectric Properties of $\text{Cu}_{0.25}\text{Tl}_{0.75}\text{Ba}_2\text{Ca}_3\text{Cu}_4\text{O}_{12-\delta}$ Superconducting Phase", *J. Supercond. Novel Magn.* **25**, 45(2012).
- [20] S. Nasri, A. L. B. Hafsia, M. Tabllout, and M. Megdiche. "Complex impedance, dielectric properties and electrical conduction mechanism of $\text{La}_{0.5}\text{Ba}_{0.5}\text{FeO}_{3-\delta}$ perovskite oxides", *Royal Soc. Chem. Adv.* **6**, 76659 (2016).
- [21] A. Benlhachemi, J. R. Gavarri, Y. Massiani, and S. Aityazza. "Studies and modeling of electrical properties of high T_c superconductor-polymer composites" *Physica C* **45**, 235(1994).
- [22] F. E. Casallas, Vera, D. Landínez, C. Parra, and J. Roa. "Structural properties, electric response and magnetic behavior of $\text{La}_2\text{SrFe}_2\text{CoO}_9$ triple complex perovskite", *In. J. Phys.* **687**, 0789(2016).
- [23] P. S Sahoo, A. Panigrahi, S. K. Patri, and R. N. P. Choudhary, "Impedance and modulus spectroscopy studies of $\text{Ba}_4\text{SrSmTi}_3\text{V}_7\text{O}_{30}$ ceramics", *Mater. Sci. Pol.* **28**, 4 (2010).
- [24] S. A. Nedil'ko, I.V. Fesych, O. G. Dzyazko, A. S. Bulachok, S. O. Solopan, and T. O. Pluatenko, "Synthesis of barium cuprate by secondary induction heating and its electrical properties", *Powder Metall. Met. Ceram.* **55**, 120 (2016).

- [25] J. Jose and M. A. Khadar, "Role of Grain boundaries on the Electrical Properties of ZnO–Ag nanocomposites, an impedance spectroscopic study" *Acta mater.* **49**, 729(2001)
- [26] J. Bashir, and R. Shaheen, "Structural and complex AC impedance spectroscopic studies of A_2CoNbO_6 ($A = Sr, Ba$) ordered double perovskites", *Solid State Science* **13**, 993(2011).
- [27] J. E. F. S. Rodrigues, C. W. A. Paschoal, E. N. Silva, K. A. Mince, and M. W. Lufaso, "Relaxation in Ba_2BiTaO_6 ceramics investigated by impedance and electric modulus spectroscopies", *Mater. Res. Bull.* **47**, 878(2012).
- [28] L. Essaleh, G. Marin, S. M. Wasim, S. Lahlali and H. Chehouani, "Analysis of complex impedance of p - $CuIn_3Se_5$ by impedance spectroscopy", *J. Alloys Compd.* **688**, 210 (2016).
- [29] J. L. Acosta, and J. R. Jurado, "High T_c superconductor polymer composite based on $YBa_2Cu_3O_{7-x}$. II. Conduction mechanisms and temperature effect on conductive and dielectric properties of polypropylene composites" *J. Appl. Polym. Sci.* **4**, 431(1995).
- [30] J. S. Lee, and H. Yoo "A New Assessment of Ionic Conductivity of $YBa_2Cu_3O_x$ via AC Impedance Spectroscopy Combined with DC Relaxation", *J. Electrochem. Soc.* **4**, 1169(1995).
- [31] H. P. Klug, and L. E. Alexander, "X-Ray diffraction procedures for polycrystalline and Amorphous materials", Wiley, (1974).
- [32] G. Gilli, "Fundamentals of Crystallography" Oxford university press, United.Kingdom. (2002).
- [33] B.E. Warren, "X-ray Diffraction" Courier corporation, United State of America (1969).
- [34] H. P. Klug, and L. E. Alexander, "X-Ray diffraction procedures: for polycrystalline and amorphous materials" 2nd ed. Wiley-interscience, New York (1974).
- [35] B.Cheney, "Introduction to scanning electron microscopy" San Jose State University press (1995).
- [36] J. Cazaux, "Mechanisms of charging in electron spectroscopy" *J. Elec. Spect. Rel. Phen.* **105**, 155(1999).
- [37] N.Unakar, J. Tsui, and C. Harding, "Scanning electron microscopy". Ophthalmic research press, United state of America. (1981).
- [38] T. G. M. Kleinpenning, "Theory of noise investigations on conductors with the four-probe method," *J. Appl. Phys.* **48**, 2946(1977).

- [40] S. M. Khetre, H. V. Jadhav, P. N. Jagdale, S. R. Kulal, and S. R. Bamane, "Studies on electrical and dielectric properties of LaFeO_3 " *Adv. Appl. Sci. Res.* **2**, 503(2011)
- [41] A. Jabbar, I. Qasim, M. Waqeur-Rehman, M. Zaman, K. Nadeem, and M. Mumtaz, "Structural and superconducting properties of $(\text{Al}_2\text{O}_3)_y/\text{CuTi-1223}$ composites", *J. Electron. Mater.* **44**, 110(2015).
- [42] M. Mumtaz, Nawzish A. Khan, and S. Khan, "Frequency dependent dielectric properties of $\text{Cu}_{0.5}\text{Tl}_{0.5}\text{Ba}_2\text{Ca}_2(\text{Cu}_{3-y}\text{M}_y)\text{O}_{10-\delta}$ superconductor", *J. Appl. Phys.* **111**, 013920(2012).
- [43] C. G. Koops "On the dispersion of resistivity and dielectric constant of some semiconductors at audio frequencies", *Phys. Rev.* **83**, 121(1951).
- [44] S. Nasri, A. L. B. Hafsia, M. Tabllout, and M. Megdiche, "Complex impedance, dielectric properties and electrical conduction mechanism of $\text{La}_{0.5}\text{Ba}_{0.5}\text{FeO}_{3-\delta}$ perovskite oxides", *Royal Soc. Chem. Adv.* **6**, 76659(2016).
- [45] H. Rahmouni, M. Smari, B. Cherif, E. Dhahri, and K. Khirouni, "Conduction mechanism, impedance spectroscopic investigation and dielectric behavior of $\text{La}_{0.5}\text{Ca}_{0.5-x}\text{Ag}_x\text{MnO}_3$ manganites with compositions below the concentration limit of silver solubility in perovskites", *J. Chem. Soc. Dalton Trans.* **44**, 10547(2015).
- [46] I. Ahmad, J. Akhtar, M. Younas, M. Saddique and M. M. Hasan, "small polaronic hole hopping mechanism and Maxwell-Wagner relaxation in NdFeO_3 ", *J. Appl. Phys.* **112**, 074105(2012).
- [47] J. Li, K. Wu, R. Jia, L. Hou, L. Gao, and S. Li, "Towards enhanced varistor property and lower dielectric loss of $\text{CaCu}_3\text{Ti}_4\text{O}_{12}$ based ceramics", *Mater. Des.* **92**,546(2016).
- [48] K. Prasad, A. Kumar, S. N. Choudhary, and R. N. P. Choudhary, "relaxor behavior of $\text{Pb}[(\text{Mg}_{2/3}\text{Co}_{1/3})_{1/3}\text{Nb}_{2/3}]\text{O}_3$ ceramic", *solid state ionics* **176**, 1641(2005).
- [49] Lily, K. Kumari, K. Prasad, and R. N. P. Choudhary, "Impedance spectroscopy of $(\text{Na}_{0.5}\text{Bi}_{0.5})(\text{Zr}_{0.25}\text{Ti}_{0.75})\text{O}_3$ lead free ceramic", *J. Alloys Compd.* **453**, 325(2008).
- [50] R. Kumari, N. Ahlawat, A. Agarwal, S. Sanghi, M. Sindhu, and N. Ahlawat, "Phase transformation and impedance spectroscopic study of Ba substituted $\text{Na}_{0.5}\text{Bi}_{0.5}\text{TiO}_3$ ceramics", *J. Alloys Compd.* **676**, 452(2016).
- [51] F. I. H. Rhouma, A. Dhahri, J. Dhahri, and M. A. Valente, "Dielectric, modulus and impedance analysis of lead-free ceramics $\text{Ba}_{0.8}\text{La}_{0.133}\text{Ti}_{1-x}\text{Sn}_x\text{O}_3$ ($x= 0.15$ and 0.2)", *Appl. Phys. A* **108**, 593(2012).
- [52] M. E. Simon and C. M. Varma, "Magnetic impurities in d-wave superconductors", *Phys. Rev. B* **60**, 9744(1999).

- [53] Z. S. Bassi, and A. LeClair, "Bound states for a magnetic impurity in a superconductor", *Physic. Rev. B* **60**, 615(1999).
- [54] S. Sen, R. N. P. Choudhary, and P. Pramanikm, "Structural and electrical properties of Ca²⁺-modified PZT electroceramics", *Phys. B Condens. Matter* **387**, 56(2007).
- [55] Ş. Çavdar, H. Koralay, and Ş. Altındal, "Effect of Vanadium Substitution on the Dielectric Properties of Glass Ceramic Bi-2212 Superconductor", *J. Low Temp. Phys.* **60**, 164(2011).
- [56] S. A. Nedilko, I. V. Fesych, O. G. Dzyazko, A. S. Bulachok, S. O. Solopan, and T. O. Plutenko, "Synthesis of Barium Cuprate by Secondary Induction Heating and its Electrical Properties" *Powder Metall. Met. Ceram.* **55**, 347(2016).